Remote Sensing of Environment 347 (2026) 115707



Contents lists available at ScienceDirect

Remote Sensing of Environment

journal homepage: www.elsevier.com/locate/rse



A scene-mapped framework for deriving clear-sky surface longwave downward radiation from remotely sensed measurements

Yihan Du [a], Tianxing Wang [b,d,e,*], Yi Zheng [a], Dahui Li [b], Yuyang Xian [b], Feiyao Gao [b], Stefan A. Buehler [c]

[a] Guangdong Provincial Key Laboratory of Geodynamics and Geohazards, School of Earth Sciences and Engineering, Sun Yat-Sen University, Zhuhai, 519000, China
[b] School of Geospatial Engineering and Science, Sun Yat-Sen University & Southern Marine Science and Engineering Guangdong Laboratory (Zhuhai), Zhuhai, 519000, China
[c] Atmospheric Science, Department of Earth System Science, Earth and Society Research Hub (ESRAH), University of Hamburg, Hamburg, Germany
[d] Key Laboratory of Comprehensive Observation of Polar Environment (Sun Yat-sen University), Ministry of Education, Zhuhai, 519082, China
[e] Key Laboratory of Natural Resources Monitoring in Tropical and Subtropical Area of South China, Ministry of Natural Resources, China

ARTICLE INFO

Keywords:
Longwave downward radiation
Brightness temperature
Lookup table
Scene mapping
MODIS
Surface energy budget
Surface–atmosphere state

ABSTRACT

Accurate estimation of clear-sky surface longwave downward radiation (LWDR) is fundamental to surface energy budget studies, yet widely used parameterizations and conventional lookup-table (LUT) searches often suffer from regional biases and limited transferability. This study develops a scene-mapped LUT framework that operates in brightness-temperature (BT) space and uses surface temperature (ST) and total column water vapor (TCWV) as physical descriptors to define scene-specific subsets and constrain spectral matching to locally consistent surface–atmosphere states. Two implementations are proposed within the scene-mapped framework: S-Poly (polynomial regression) and S-LUT (sub-LUT distance search). Validation against multi-network ground measurements using MODIS inputs yielded RMSEs of 26.36 and 26.89 W m^{-2} and biases of −0.86 and −2.75 W m^{-2} for S-LUT and S-Poly, respectively. The corresponding RMSEs were lower than those of the global-LUT benchmark (29.26 W m^{-2}) and the evaluated general clear-sky parameterization benchmark (30.03 W m^{-2}), representing reductions of 12.2% and 10.5% relative to the latter. Both methods generally maintained stable accuracy across diverse surface types and climatic regions. S-LUT was more consistent across the evaluated configurations and achieved an RMSE of 22.48 W m^{-2} under the mixed MODIS–ERA5 configuration. The flexible scene-mapping framework may also provide a useful methodological concept for adapting radiation retrieval to different sensors and exploring future extensions toward all-sky conditions.

1. Introduction

The longwave greenhouse effect regulates Earth's climate (Wang and Dickinson, 2013; Wild et al., 2013). Longwave downward radiation (LWDR) is a crucial component of Earth's surface energy balance and is pivotal for understanding climate change, as well as land surface, atmospheric, and oceanic circulations (Liang et al., 2019; Lopes et al., 2024; Stephens et al., 2012; Xu et al., 2026). With continuing advances in Earth observation, satellite remote sensing has become an essential tool for regional and global LWDR estimation and long-term data production (Guo et al., 2024; Jiao and Mu, 2022; Zeng et al., 2024).

During the development of LWDR estimation methods, radiative transfer models (RTMs) have been widely employed owing to their rigorous physical basis (Berk et al., 2015; Vicent et al., 2020). However, their dependence on detailed atmospheric and surface inputs and repeated forward calculations constrains direct application to large-scale and long-term retrievals (Zhang et al., 2022). Lookup-table (LUT) methods precompute radiative transfer under various atmospheric and surface conditions using RTMs and store the results in LUTs, enabling rapid and accurate retrieval of LWDR without the need for repeated costly simulations (Liang et al., 2021; Servera et al., 2019). Thus, LUTs serve as an efficient surrogate to direct RTM calculations, balancing physical fidelity with computational efficiency. However, while LUT methods are highly efficient during the retrieval phase, their

* Corresponding author at: School of Geospatial Engineering and Science, Sun Yat-Sen University & Southern Marine Science and Engineering Guangdong Laboratory (Zhuhai), Zhuhai 519000, China.
E-mail address: wangtx23@mail.sysu.edu.cn (T. Wang).

https://doi.org/10.1016/j.rse.2026.115707
Received 28 February 2026; Received in revised form 24 September 2026; Accepted 25 September 2026
Available online 2 October 2026
0034-4257/© 2026 Elsevier Inc. All rights are reserved, including those for text and data mining, AI training, and similar technologies.

construction phase remains computationally expensive (Servera et al., 2019). The high dimensionality and substantial computational cost associated with these tables pose a critical bottleneck for algorithm development (Li et al., 2024; Vicent et al., 2020).

As the demand for LWDR estimation increased, simplified statistical approaches gradually became dominant, particularly parameterization schemes and machine learning techniques. Parameterization methods typically estimate atmospheric emissivity based on surface meteorological observations, such as air temperature and humidity, applying the Stefan–Boltzmann law to compute LWDR (Idso, 1981; Prata, 1996). Their simplicity and computational efficiency have led to widespread adoption in global-scale applications (Cheng et al., 2017; Jiao and Mu, 2022; Yu et al., 2022; Zhou et al., 2019). Nevertheless, these methods heavily depend on the spatial and temporal representativeness of training samples, exhibit variability across different models, and often suffer from limited transferability of regression coefficients across diverse climatic regions, thereby constraining their global applicability (Chauhan et al., 2025; Jiao and Mu, 2022; Pace et al., 2024). More recently, machine learning methods, including deep learning, have gained prominence in the remote sensing community by leveraging large-scale datasets to capture complex nonlinear relationships, thereby improving retrieval accuracy (Chauhan et al., 2025; Feng et al., 2020; Guo et al., 2024; Xu et al., 2026; Xu et al., 2022; Xu et al., 2023; Zhou et al., 2019; Zhu et al., 2022). However, these data-driven models generally lack physical interpretability and are highly sensitive to the representativeness of training data, making data dependency a critical bottleneck in LWDR estimation (Reichstein et al., 2019).

To overcome these challenges, hybrid methods have emerged as an effective solution. These methods integrate the physical accuracy of RTMs with the efficiency of statistical models, thereby enabling more reliable radiation retrieval under complex atmospheric conditions (Cheng et al., 2017; Liang et al., 2010; Tang and Li, 2008; Wang and Liang, 2009, 2010). By utilizing top-of-atmosphere (TOA) observations of brightness temperature (BT) or radiance, hybrid methods directly retrieve surface longwave radiation flux, effectively bypassing the error propagation typically associated with atmospheric parameter retrieval in traditional methods (Cheng et al., 2017). Recent studies have demonstrated the effectiveness of hybrid approaches for clear-sky LWDR retrieval by combining radiative-transfer simulations with satellite thermal-infrared observations and auxiliary atmospheric information (Jiao and Mu, 2022; Yu et al., 2022; Yu et al., 2019). In practice, such approaches use simulated or observational datasets to establish mappings from multi-band TOA observations (typically radiances) to surface LWDR (Jiao and Mu, 2022; Zhou et al., 2019; Zhu et al., 2022). However, as the number of possible channel and auxiliary-variable combinations increases, identifying stable and transferable mappings becomes increasingly challenging. Recent studies have further shown that LWDR estimation performance can be strongly dependent on atmospheric and surface conditions. Air-temperature inversions can substantially degrade the accuracy of commonly used clear-sky parameterization schemes (Cheng et al., 2020). In polar regions, clear-sky LWDR retrievals and model evaluations have also revealed substantial performance differences across products and environmental conditions (Guo et al., 2024; Pace et al., 2024). Similar model dependence has been reported over complex high-elevation terrain in the Himalayas (Chauhan et al., 2025). Taken together, these findings suggest that globally fixed or weakly stratified retrieval relationships may not fully represent the diversity of atmospheric and surface states, motivating retrieval strategies that explicitly constrain the local physical state space.

In parallel, scene-classification approaches have been introduced to better account for regional and climatic diversity in longwave radiation retrieval. The Clouds and the Earth's Radiant Energy System (CERES) mission, for instance, employs Angular Distribution Models (ADMs) that stratify radiative anisotropy by scene type to convert measured radiances to TOA fluxes (Loeb et al., 2005; Loeb et al., 2007; Su et al., 2015). Building on this principle, Doelling et al. (2016) developed a radiance-based algorithm (RBA) to derive longwave fluxes from geostationary satellites. The RBA defines scenes using window and water-vapor channel radiances, viewing geometry, day–night separation, and auxiliary parameters such as cloud cover and surface type, and is now widely applied in the CERES SYN1deg product chain. More recently, Li et al. (2024) advanced this concept by proposing the Multi-Dimensional Matrix MAPping (MDMAP) for outgoing longwave radiation (OLR) retrieval, which incorporates scene classification and differential absorption principles to establish mappings between TOA BT observations and OLR. Conceptually, these scene-mapping approaches share a common logic with LUT-based methods: both precompute and store large sets of radiative quantities through RTM simulations and subsequently reduce computational cost through efficient look-up operations. By balancing physical consistency with computational efficiency, such approaches enable accurate radiative-flux estimation across a wide range of atmospheric and surface conditions. These studies provide precedents for scene-stratified radiative mapping and efficient look-up.

Building on the general principles of hybrid retrieval and scene classification, this study develops a new framework for surface LWDR estimation. Specifically, the proposed scene-mapped LUT strategy uses surface temperature (ST) and total column water vapor (TCWV) as physical descriptors of surface–atmosphere state (Cheng et al., 2017; Wang et al., 2023; Wang et al., 2020). By using these descriptors to define scene-specific subsets of the LUT and restricting the retrieval to the corresponding local state space, the framework constrains spectral matching to physically relevant surface–atmosphere conditions and reduces the effective retrieval search space.

2. Data

2.1. Remote sensing observation data

(1) MODIS

MODIS sensors aboard the Terra and Aqua platforms provide high spatial resolution observations of surface and atmospheric parameters at the global scale (Toller et al., 2013). In this study, ten longwave spectral channels from the MODIS Level-1B radiance products MOD/MYD02SSH were selected as the primary inputs (Table 1). These products provide calibrated radiances subsampled to 5 km at nadir. Scene classification was performed using ST (from MOD11) and TCWV (from MOD05) as the primary stratification variables, with clear-sky conditions identified from MOD35 for the MODIS-only configuration (King et al., 2013; Wan, 2014). ST from MOD/MYD06 (using only pixels with zero cloud fraction) was additionally used to facilitate comparison in Section 4.3 with existing LWDR products that adopt MOD/MYD06 as a unified ST input and to support global application, including over oceanic regions where MOD11 is unavailable.

(2) CERES-SSF

Table 1
MODIS channels used for simulations.

Band	Bandwidth (μm)	Central wavelength (μm)	Required NE△T (K)	Primary use
27	6.535–6.895	6.770	0.25	Cirrus Clouds
28	7.175–7.475	7.343	0.25	Water Vapor
29	8.400–8.700	8.529	0.05	Cloud Properties
30	9.580–9.880	9.735	0.25	Ozone
31	10.780–11.280	11.012	0.05	Surface/Cloud
32	11.770–12.270	12.033	0.05	Temperature
33	13.185–13.485	13.365	0.25	Cloud Top
34	13.485–13.785	13.684	0.25	Altitude
35	13.785–14.085	13.912	0.25	
36	14.085–14.385	14.196	0.35	

CERES Single Scanner Footprint (SSF) product provides footprint-level measurements and derived radiative flux products from CERES observations. The product includes geolocated radiative quantities together with viewing geometry, cloud properties, and surface parameters for each CERES footprint. In this study, the Model B surface downward longwave flux was extracted from CERES-SSF. CERES-SSF is a well-established product for surface radiation studies, and its surface longwave flux algorithms have been extensively evaluated and applied in previous studies (Gupta et al., 2010). Because CERES and MODIS are carried on the same Terra platform, and MODIS scene information is incorporated into the CERES-SSF processing, the two datasets can be conveniently collocated for spatial comparison.

2.2. Reanalysis data

ERA5, produced by the European Centre for Medium-Range Weather Forecasts (ECMWF), provides hourly global atmospheric and surface parameters at 0.25° spatial resolution by assimilating satellite and in situ observations within a consistent modeling system, ensuring globally consistent and spatially complete coverage (Hersbach et al., 2020). In this study, ERA5 TCWV was used as an alternative scene-classification variable to evaluate the framework under a mixed-source input configuration.

2.3. Ground measurements

To ensure reliable validation of the LWDR retrievals, quality-controlled in situ measurements were collected from 109 land and ocean stations across six observation networks: AmeriFlux (Novick et al., 2018), the Baseline Surface Radiation Network (BSRN) (Driemel et al., 2018), the Tibetan Plateau Land–Atmosphere Interaction Observational Network (TPLAI) (Ma et al., 2024), AsiaFlux (Yu and Hirano, 2021), the Tropical Atmosphere Ocean (TOGA-TAO) array (Mangum et al., 1994), and OceanSITES (Cronin et al., 2023; Weller et al., 2022).

During station selection, duplicate and closely located stations were removed within and across the observation networks. This screening reduced redundant sampling of the same local area at the MODIS pixel scale. To reduce geographical clustering while preserving environmental diversity, densely distributed land-station candidates were spatially screened and sampled across Köppen climate zones (Beck et al., 2018) and IGBP surface types (Friedl et al., 2010). For spatial collocation, the nearest satellite pixel was assigned to each station, and only matchups with a station-to-pixel-center distance of no more than 7.5 km were retained.

Validation matchups were constructed at discrete valid MODIS overpasses, with one matchup retained for each station and valid overpass. Ground observations were matched directly to satellite overpass times where possible; otherwise, values were interpolated from valid bracketing records. Network-provided quality flags were applied, and missing, invalid, or physically implausible LWDR observations were excluded. Together, these observations cover diverse climatic regions and surface types and provide an independent basis for evaluating the LWDR retrievals. Their geographical distribution is shown in Fig. 1.

2.4. Auxiliary data

The Thermodynamic Initial Guess Retrieval (TIGR) dataset (Chedin et al., 1985; Chevallier et al., 1998) provides a widely used set of atmospheric profiles for radiative transfer applications. The profiles were constructed from radiosonde observations and subjected to strict quality control, offering a curated and diverse profile set that spans five air-mass categories and is widely used in radiative-transfer applications (Li et al., 2024; Wang et al., 2020; Wang et al., 2012; Zheng et al., 2022). The dataset comprises 2311 atmospheric profiles, classified into five air mass categories: tropical, mid-latitude 1, mid-latitude 2, polar 1, and polar 2. Among them, 946 profiles correspond to clear-sky conditions and are commonly employed in radiative transfer simulations. To construct a representative subset for LUT simulations, atmospheric profiles were selected by jointly considering atmospheric bottom-layer temperature (T_0), TCWV, the vertical structures of temperature and water vapor, air-mass category, and temperature-inversion characteristics (Aires and Prigent, 2007; Cheng et al., 2020; Chevallier et al., 2000; Dupont et al., 2008; Zheng et al., 2022). This multidimensional selection resulted in 113 representative clear-sky TIGR profiles covering all five air-mass categories and a broad range of atmospheric conditions (Fig. 2 a–c).

The ECOSTRESS spectral library provides thousands of laboratory-measured emissivity spectra covering a broad range of natural and artificial materials, including vegetation, soils, rocks, minerals, water, snow and ice, and man-made surfaces, thereby supporting detailed

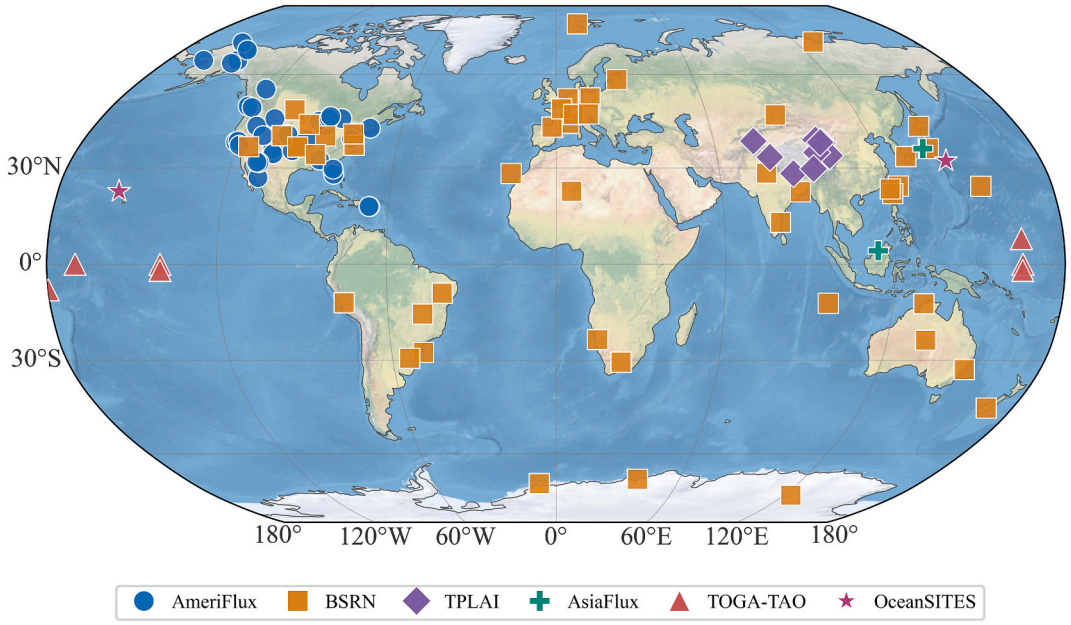


Fig. 1. Global distribution of ground-based observation sites used for validation.

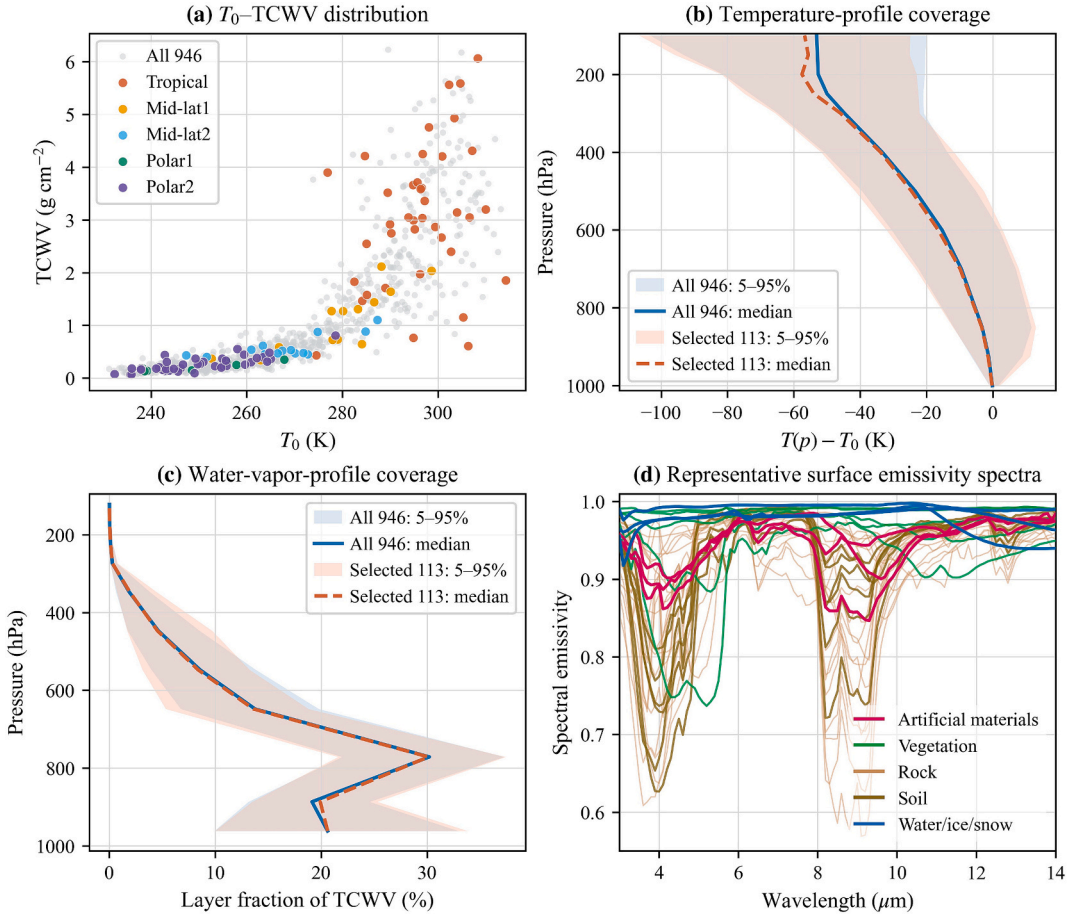


Fig. 2. Atmospheric-profile and surface-emissivity representation for LUT construction. (a) T_0–TCWV distribution of the 946 TIGR clear-sky profiles and the 113 selected profiles. (b) Median and 5th–95th percentile ranges of temperature profiles. (c) Median and 5th–95th percentile ranges of vertical water-vapor distributions. (d) The 38 representative ECOSTRESS surface emissivity spectra.

characterization of surface thermal properties (Meerdink et al., 2019). Data from spectral libraries have been widely applied in studies of surface energy balance and radiative transfer (Lelli et al., 2023; Li et al., 2024; Ru et al., 2023; Wang et al., 2024). The library covers approximately 0.35–15.4 μm. Because it integrates spectra from multiple source libraries and instruments, the native spectral sampling varies among individual records. For LUT construction, 38 representative emissivity spectra were selected by considering major surface categories together with their MODIS-band response-weighted emissivity characteristics, while retaining spectrally distinct and extreme cases. The selected spectra span artificial materials, vegetation, rocks, soils, and water/ice/snow surfaces, and their spectral diversity is illustrated in Fig. 2d.

3. Methods

3.1. MODTRAN-based simulation

The simulation database was generated using MODTRAN6 (Berk et al., 2015) to simulate clear-sky LWDR and corresponding top-of-atmosphere thermal radiances under diverse atmospheric, surface, and viewing conditions. The parameter settings for LUT construction are summarized in Table 2.

TCWV simulation nodes were adaptively defined for each atmospheric profile to balance radiative sensitivity and LUT size. The resulting profile-dependent TCWV sampling, constrained by the corresponding saturation limits, is shown in Fig. 3.

An independent validation dataset was generated using the simulation parameters listed in Table 3. Continuous variables were randomly sampled within the specified ranges, while all other parameters were consistent with Table 2 or retained at their default MODTRAN settings. Physically unrealistic cases, including supersaturated clear-sky conditions, were excluded.

Table 2
MODTRAN parameter settings for simulating clear-sky LWDR LUT.

Parameters	Setting
Viewing zenith angle	0°, 11.5°, 23°, 33°, 42°, 48.5°, 55°, 60.5°, 65°
Atmospheric profiles	113 representative profiles selected from 946 clear-sky TIGR profiles
Surface emissivity	38 representative spectra from the ECOSTRESS spectral library
Land surface temperature (K)	ST ∈ [T_0 − 10 K, T_0 + 20 K] at 5 K intervals; extended to T_0 − 25 K or T_0 + 25 K for extreme profiles
Spectral setting	4–200 μm at 1 cm^{-1}
Aerosol	(Default) Rural, VIS = 23 km
Water vapor (g/cm^2)	Profile-dependent adaptive nodes within the profile-specific saturation and physical limits; midpoint LWDR interpolation error ≤ 1 W m^{-2}
CO_2 (ppm)	400

3.2. Identification of the optimal channel subset

In LUT-based LWDR retrievals, increasing the number of BT channels does not necessarily yield monotonic improvements in accuracy (Tang and Li, 2008). Extra channels may increase dimensionality and redundancy without providing additional retrieval information. Therefore, an

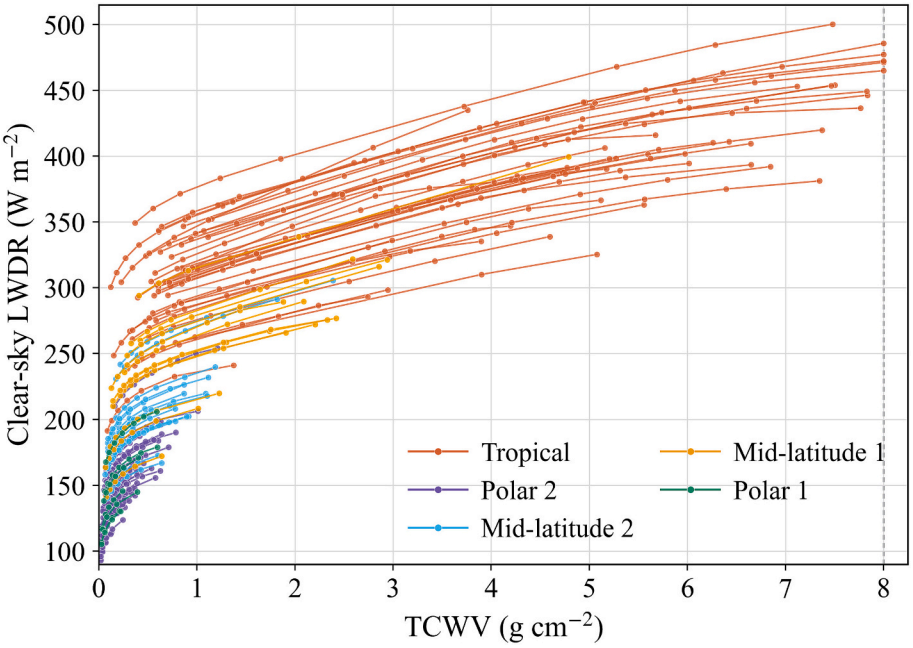


Fig. 3. Clear-sky LWDR responses to TCWV for representative atmospheric profiles. The TCWV range of each profile is constrained by its physical and saturation limits.

Table 3
MODTRAN parameter settings for the validation dataset.

Parameters	Setting
Viewing zenith angle	VZ ∈ [0°, 65°]
Atmospheric profiles	Randomly sampled from the remaining TIGR clear-sky profiles
Surface emissivity	Randomly sampled from the remaining ECOSTRESS spectral library
Land surface temperature (K)	ST ∈ [$T_o - 15$ K, $T_o + 15$ K]
Water vapor (g/cm^2)	TCWV ∈ [0.004, min(8, profile saturation limit)]

Note: Values were randomly sampled within the specified ranges for simulation. Samples with input parameter combinations already used for LUT construction or parameter tuning were excluded from the validation dataset.

optimal channel subset was selected by jointly considering retrieval accuracy and stability.

Candidate channel subsets were evaluated using a basic LUT retrieval scheme. The simulation database was divided into view zenith angle (VZ) bins, and for each query sample, the nearest neighbor was identified within the corresponding bin by minimizing a Mahalanobis distance in the selected BT subspace:

$$d = \sqrt{\left(BT^{query} - BT^{ref}\right)^T \Sigma^{-1} \left(BT^{query} - BT^{ref}\right)} \quad (1)$$

where Σ denotes the covariance matrix of the candidate channels. The LWDR of the nearest match was then assigned to the query. Retrieval performance was evaluated using three repeats of five-fold cross-validation grouped by atmospheric profile, ensuring that samples derived from the same atmospheric profile were retained within the same fold. Channel combinations were refined in a forward–backward manner, and their performance and stability were evaluated across the different viewing angles and TIGR air-mass categories. This procedure identified BT29, BT31, BT32, and BT33 as the most informative and stable four-channel set.

3.3. Baseline LUT retrieval methods

The traditional LUT method estimates LWDR by searching for the most similar entries within a pre-constructed reference table, typically using Euclidean distance between the target record and LUT entries. This approach provides a straightforward mapping from satellite-observed variables to LWDR but relies heavily on the density and representativeness of the LUT, and brute-force search becomes computationally prohibitive for large datasets. In this study, an efficient Euclidean distance search was implemented using KDTree, combined with feature standardization to balance the contributions of predictors with different scales.

Two traditional LUT-based configurations were evaluated. For clarity, they are denoted as T-Global (global search) and T-Cascade (cascade search). The retrieval settings were selected from candidate values based on retrieval accuracy and computational efficiency.

(1) T-Global (Global Search)

In this variant, all predictors (VZ, ST, TCWV, and the BT of selected channels) are jointly included in a KDTree search. For each observation, a fixed number of nearest neighbors (60 in this study) are retrieved, and LWDR is estimated by inverse-distance weighted averaging, with the weights determined by distances in the selected BT space.

(2) T-Cascade (Cascade search)

Inspired by scene-mapping, a KDTree search is first performed in the standardized angular and atmospheric dimensions (VZ, ST, and TCWV) to identify the 1200 closest LUT entries. A second KDTree search is then performed in the BT space, and the closest 5% of entries are retained. LWDR is estimated using the same inverse-distance weighting scheme as T-Global.

T-Cascade was included as an intermediate state-conditioned baseline. It introduces a soft scene constraint through fixed-size nearest-neighbor preselection in the VZ–ST–TCWV space, but, unlike the proposed scene-mapped methods, it does not construct an explicitly bounded local thermodynamic state space.

3.4. Scene-mapping LWDR retrieval method

Surface LWDR is governed by coupled surface–atmosphere processes. To reduce ambiguity in spectral matching, scenes are defined by viewing geometry and thermodynamic state, and LWDR is retrieved within scene-constrained subsets of the LUT. The overall procedure is illustrated in Fig. 4.

For scene mapping, the TCWV dimension is represented by $W = \ln(1 + TCWV)$, while TCWV remains the physical moisture descriptor. For each target pixel, VZ is first assigned to a discrete bin $\left[VZ_i^L, VZ_{\{i+1\}}^L\right]$. To mitigate bin-edge effects and quantization mismatches, the search window is then expanded along the ST and transformed-TCWV dimensions around the corresponding LUT bin centers $\left(ST_j^L, W_k^L\right)$ using asymmetric coefficients:

$$ST^L \in \left[ST_j^L - a_{ST}\cdot\Delta ST, ST_j^L + b_{ST}\cdot\Delta ST\right] \quad (2)$$

$$W^L \in \left[W_k^L - a_{TCWV}\cdot\Delta W, W_k^L + b_{TCWV}\cdot\Delta W\right] \quad (3)$$

where ΔST and ΔW define the reference scales along the ST and trans-

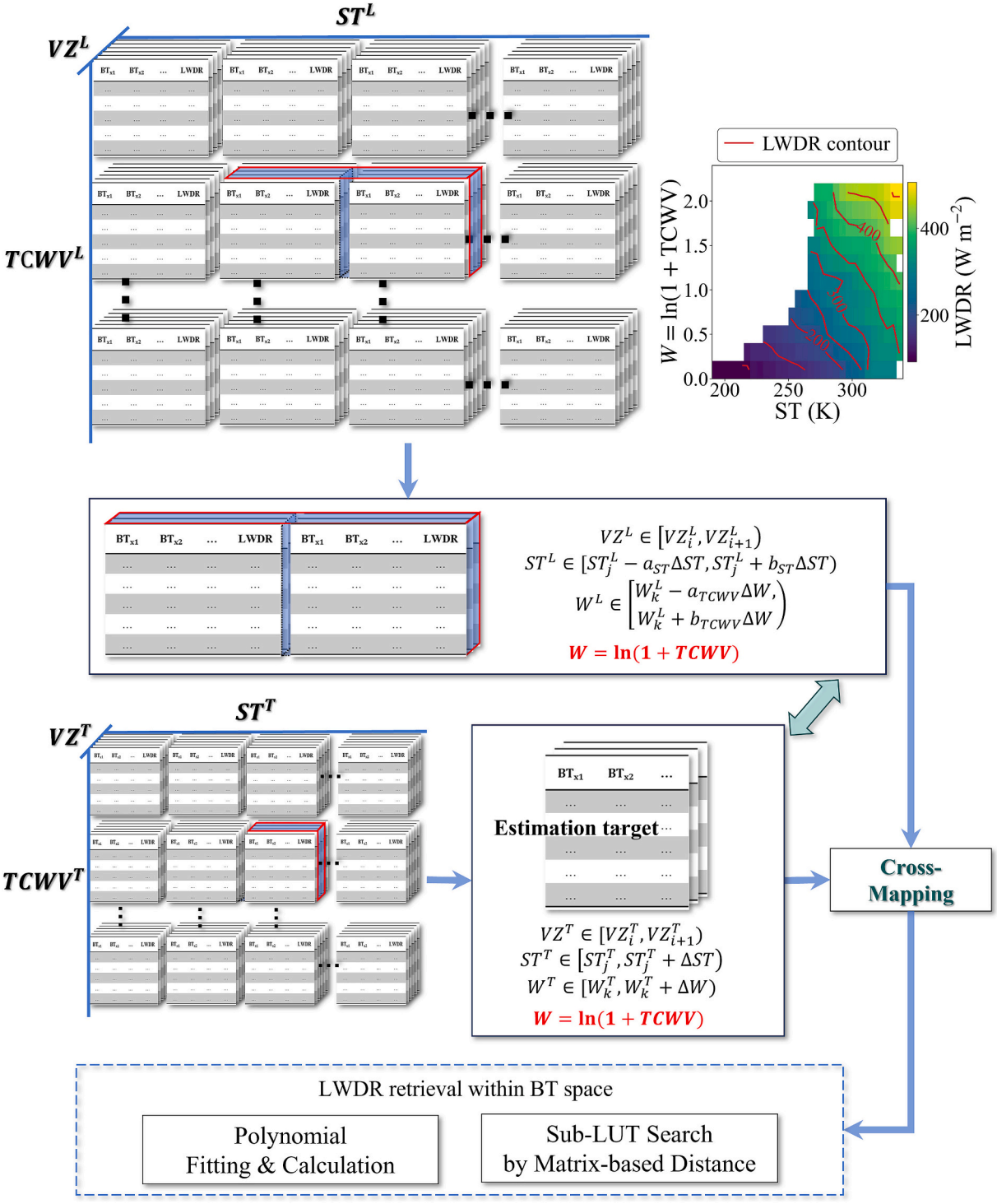


Fig. 4. Workflow of the scene-mapping method for LWDR retrieval. Superscript L denotes LUT, while superscript T denotes target.

formed TCWV dimensions, respectively, while a_{ST}, b_{ST}, a_{TCWV}, and b_{TCWV} are signed coefficients controlling their asymmetric expansion. Negative values shift the corresponding window boundary across the nominal ST or moisture-state bin center, allowing the search to adapt to asymmetric thermodynamic-state distributions. The coefficients are constrained to $-3 \le a, b \le 3$ and $1 < a + b \le 3$, ensuring a valid window width while limiting excessive expansion. This yields a scene-specific candidate subset $L_{\{i,j,k\}}$ that is physically consistent with the target pixel.

In practice, ΔST and ΔW were determined by jointly considering the sampling characteristics of the simulated LUT, retrieval performance, and the resulting sub-LUT size in parameter-sensitivity tests. Since the actual search range is further adjusted by the asymmetric expansion coefficients, $\Delta ST = 5$ K and $\Delta W = 0.20$ were adopted as the reference scales in this study. For LUTs with non-uniform sampling, the effective search range can be further adapted to the local sampling density, for example by determining the expansion coefficients separately for different sampling regimes.

The asymmetric expansion is controlled by coefficient pairs $\{a_{ST}, b_{ST}\}$ and $\{a_{TCWV}, b_{TCWV}\}$. Their optimal values were determined through a three-stage iterative search (coarse grid with step size 2: {−3,−1,1,3}; integer neighborhood around the optimum: {opt−1, opt, opt+1}; half-step refinement: {opt−0.5, opt, opt+0.5}), with iterations proceeding under these constraints until the minimum RMSE is reached. Although smaller step sizes could in principle further improve precision, the current step size already provides a balanced compromise between efficiency and accuracy.

After scene mapping, LWDR retrieval is restricted to a smaller LUT subset representing similar surface–atmosphere conditions, thereby reducing cross-scene ambiguity. Target pixels assigned to the same VZ–ST–TCWV scene are processed jointly in matrix form, avoiding repeated pixel-wise operations and enabling efficient batch retrieval for both scattered observations and full images. Two implementations of the scene-mapping framework were tested. For clarity, they are denoted as S-Poly (polynomial regression) and S-LUT (sub-LUT distance search):

(1) S-Poly (polynomial regression)

Within each scene-specific subset, S-Poly establishes statistical relationships between channel BTs and LWDR. The framework can accommodate different polynomial formulations depending on the application, while a first-order form is adopted in this study to balance retrieval accuracy and computational efficiency. LWDR is therefore expressed using the selected BT channels as predictors:

$$LWDR = d_0(VZ, ST, TCWV) + \Sigma_{x_i}\, d_{x_i}(VZ, ST, TCWV) \cdot BT_{x_i} \tag{4}$$

where d_0 is the scene-dependent intercept and d_i are the regression coefficients for each BT channel. BT_{x_i} denotes the BT of the specified spectral channel.

(2) S-LUT (Sub-LUT distance search)

Within each scene-specific LUT subset, S-LUT identifies the closest entries to the target observations in the selected BT space using KDTree. The nearest 15% are retained, and their LWDR values are combined using inverse-distance weighting. The neighbor proportion was selected from candidate settings based on retrieval accuracy and stability.

3.5. General clear-sky parameterization models

Under clear-sky conditions, LWDR is typically estimated using parameterization models that establish empirical or semi-empirical relationships with satellite-observed thermal radiances, ST, TCWV, and related variables. Following the comparative evaluation of representative clear-sky LWDR models by Jiao and Mu (2022), three well-performing parameterizations were selected as benchmarks to enable a consistent comparison with the retrieval methods evaluated in this study.

(1) Wang2023 general parameterization

This generalized approach replaces radiance combinations with only two predictors: ST and TCWV. By using polynomial terms of logarithmic functions of TCWV, the model accounts for nonlinear absorption effects of water vapor (Wang et al., 2020). The formulation is:

$$\begin{aligned} LWDR = {} & A_0 + A_1 \times ST^{a_0} \times \ln(1 + TCWV)^{a_1} + A_2 \\ & \times \ln(1 + TCWV)^{a_2} + A_3 \times \ln(1 + TCWV)^{a_3} \end{aligned} \tag{5}$$

where A_i, a_i are empirically determined regression coefficients. The latest coefficient set reported by Wang et al. (2023) was adopted in this study.

(2) Tang2008 linear radiance-based model

This model applies a linear combination of several MODIS TIR channel radiances to estimate LWDR (Tang and Li, 2008). The regression coefficients are predefined for different VZ and surface elevations, typically organized in the form of a look-up table. Its formulation is:

$$LWDR = b_0 + b_{28}L_{28} + b_{29}L_{29} + b_{31}L_{31} + b_{33}L_{33} + b_{34}L_{34} + b_{36}L_{36} \tag{6}$$

where L_i represents the TOA spectral radiance of MODIS band i, and b_i denotes the corresponding regression coefficient. The coefficients vary with VZ and surface elevation and are adopted from Jiao and Mu (2022).

(3) Wang2009 nonlinear radiance-based model

This model extends the linear form by incorporating surface air temperature (expressed through thermal radiance) and several nonlinear terms of MODIS TIR channels (Wang and Liang, 2009). Surface elevation is also included to reflect pressure effects, with coefficients varying by viewing geometry. The model can be written as:

$$\begin{aligned} LWDR = L_{T_{air}} \Bigg(& c_0 + c_1 L_{27} + c_2 L_{29} + c_3 L_{33} + c_4 L_{34} \\ & + c_5 \left(\frac{L_{32}}{L_{31}}\right) + c_6 \left(\frac{L_{33}}{L_{32}}\right) + c_7 \left(\frac{L_{28}}{L_{31}}\right) + c_8 H \Bigg) \end{aligned} \tag{7}$$

where L_i denotes the radiance of channel i, $L_{T_{air}}$ represents air temperature expressed in radiance units, and H is surface elevation in kilometers. $L_{T_{air}}$ was approximated by L_{32} during daytime and L_{31} at night. The coefficients c0–c8 are adopted from Jiao and Mu (2022).

4. Results

4.1. Validation against simulated data

The four LUT-based retrieval variants were first evaluated using the MODTRAN-simulated dataset described in Section 3.1. The four methods apply different levels of constraint to the LUT search. T-Global searches the full LUT. T-Cascade serves as an intermediate benchmark between global search and explicit scene mapping. It first limits the candidate set using VZ, ST, and TCWV. However, it does not construct the explicitly bounded scene windows used by S-LUT and S-Poly.

All methods show close agreement with the simulated LWDR reference (Fig. 5), with R values ranging from 0.987 to 0.989. The scene-mapping methods achieve lower retrieval errors than the two baseline LUT approaches. S-Poly performs best, with an RMSE of 13.10 W m^{-2}, followed by S-LUT with 13.80 W m^{-2}, compared with 14.50 and 14.80 W m^{-2} for T-Cascade and T-Global, respectively. The scene-mapping methods also substantially reduce systematic bias, with biases of 0.56 W m^{-2} for S-Poly and 0.16 W m^{-2} for S-LUT, compared with

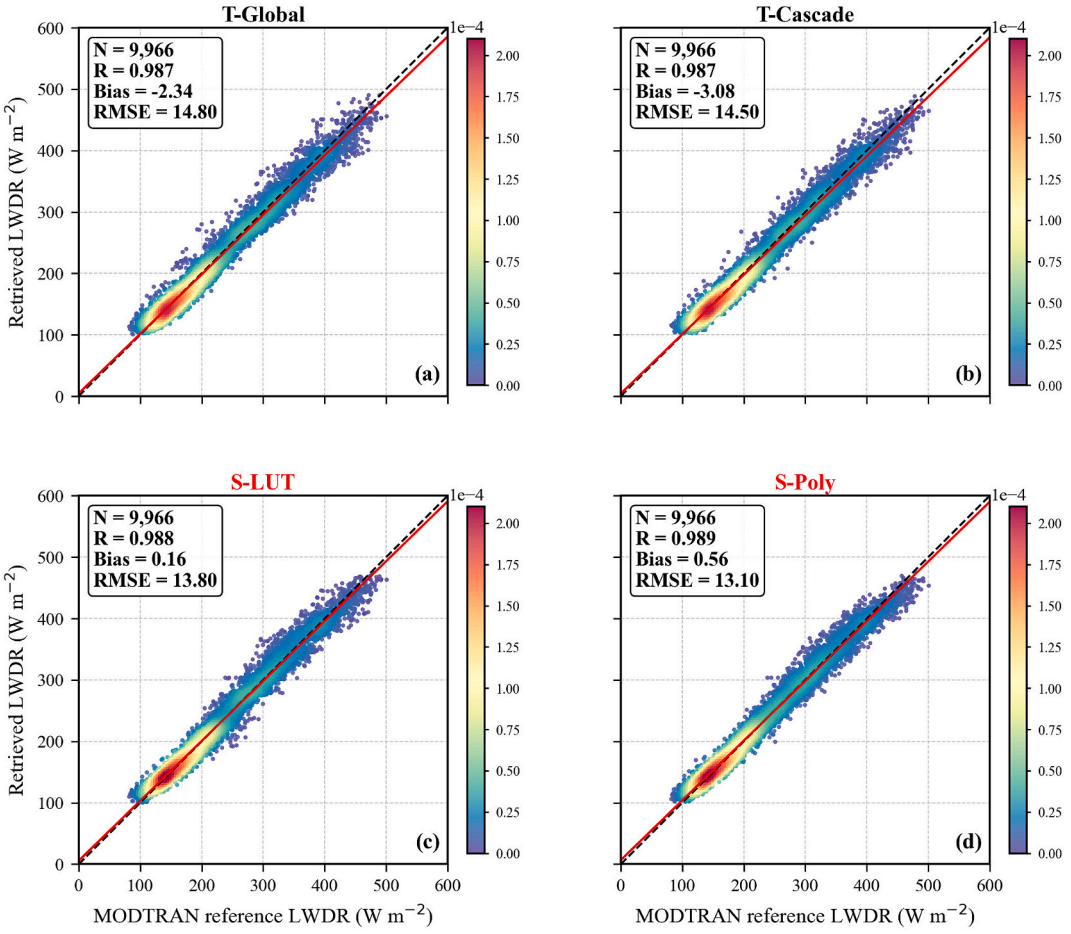


Fig. 5. Validation of LWDR retrieval methods against MODTRAN-simulated data: (a) T-Global, (b) T-Cascade, (c) S-LUT, and (d) S-Poly.

−3.08 and − 2.34 W m^{-2} for T-Cascade and T-Global. T-Cascade reduces RMSE by 2.0% relative to T-Global, but the magnitude of its negative bias increases. Relative to T-Cascade, S-LUT and S-Poly reduce RMSE by 4.8% and 9.7%, respectively. Their absolute biases decrease by 94.8% and 81.8%, respectively. This stepwise comparison indicates that explicit scene mapping provides added value beyond cascade preselection.

To further examine the robustness of the retrieval strategies, synthetic perturbations of increasing magnitude were added to the BT inputs (Fig. 6). Retrieval accuracy gradually decreases with increasing perturbation for all four methods, but the scene-mapping approaches consistently outperform the traditional LUT methods. S-Poly maintains the lowest RMSE and highest correlation across all tested perturbation levels, while S-LUT consistently provides the second-best performance. T-Cascade retains lower RMSE and higher correlation than T-Global at all perturbation levels. However, it remains less accurate than S-LUT and S-Poly.

The two scene-mapping implementations nevertheless exhibit different responses to increasing BT perturbations. S-LUT shows the smallest increase in RMSE across the tested range, indicating greater

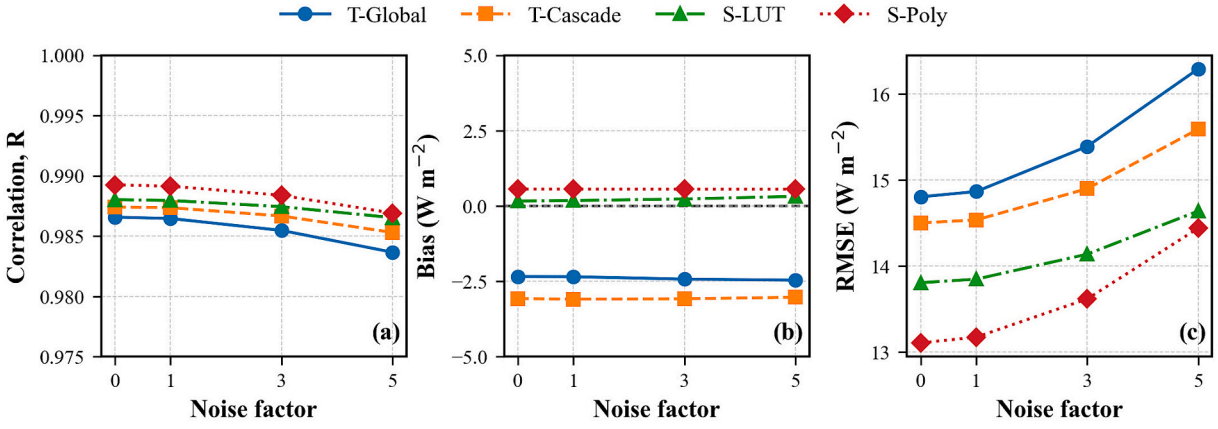


Fig. 6. Impact of synthetic BT noise on the retrieval performance of the four LUT-based methods. Correlation (a), bias (b), and RMSE (c) are evaluated under noise factors of 0, 1, 3, and 5.

robustness to BT perturbations, whereas S-Poly provides the highest absolute retrieval accuracy throughout the experiment. Both scene-mapping methods also maintain small and stable biases as perturbation increases. These results suggest complementary characteristics of the two implementations: S-Poly favors retrieval accuracy, whereas S-LUT provides greater stability against increasing BT uncertainty.

Additional sensitivity tests showed that, within realistic auxiliary-data uncertainty ranges, errors in ST and TCWV did not lead to substantial nonlinear amplification of the final LWDR retrieval error. The scene-mapping methods also maintained stable retrieval accuracy under low-level temperature-inversion conditions, with only moderate increases in retrieval error as inversion strength increased.

4.2. Validation against ground-based observations

4.2.1. Overall retrieval performance

The retrieval strategies were further evaluated against ground-based LWDR measurements to assess their performance under actual satellite observations (Fig. 7). In this evaluation, all radiances and BTs were consistently obtained from MOD02SSH. ST and TCWV were obtained from MOD11 and MOD05, respectively. For comprehensive comparison, three clear-sky parameterization models described in Section 3.5 (Tang2008, Wang2009, and Wang2023) were also included.

R values remain consistently high across all methods, ranging from 0.95 to 0.96. Parameterization models show larger retrieval errors and generally stronger negative biases. Wang2009 yields an RMSE of 31.28 $W m^{-2}$ and a bias of −7.54 $W m^{-2}$. Tang2008 produces an RMSE of 29.81 $W m^{-2}$ but shows the largest underestimation, with a bias of −13.07 $W m^{-2}$. Wang2023 yields an RMSE of 30.03 $W m^{-2}$ and a bias of −4.17 $W m^{-2}$. The traditional LUT methods provide moderate improvements, with RMSEs of 29.26 $W m^{-2}$ for T-Global and 28.66 $W m^{-2}$ for T-Cascade. The scene-mapping methods achieve the lowest overall errors. S-LUT performs best, with an RMSE of 26.36 $W m^{-2}$ and a bias of −0.86 $W m^{-2}$, followed by S-Poly with an RMSE of 26.89 $W m^{-2}$ and a bias of −2.75 $W m^{-2}$. Relative to Wang2023, S-LUT and S-Poly reduce RMSE by approximately 12.2% and 10.5%, respectively. These results indicate that incorporating scene-mapping improves overall retrieval accuracy and reduces systematic bias under real observational conditions.

4.2.2. Performance across surface types and climatic regions

Across different land-cover categories, the retrieval strategies exhibit distinct strengths (Fig. 8). Parameterization models exhibit systematic underestimation, most notably Tang2008, while Wang2023 shows relatively better performance but still suffers from significant negative biases over snow and ice surfaces. Such parameterizations can perform differently across seasons and regions; their simplified functional forms may partly contribute to this variability (Trigo et al., 2010). In contrast, LUT-based approaches generally outperform parameterization schemes by leveraging radiative transfer–based lookup tables, thereby reducing systematic biases and confining RMSE to below ~30 $W m^{-2}$ for most land cover types.

Although the relative ranking varies among individual land-cover classes, the LUT-based methods generally maintain stable performance across different surface types. Within this group, the scene-mapping methods achieve lower RMSEs and smaller biases for most land-cover classes. Their advantages are particularly evident over urban and built-up areas, snow and ice, and barren or sparsely vegetated surfaces. S-LUT shows especially low errors over snow and ice and barren surfaces, whereas S-Poly performs slightly better over several vegetation-dominated classes, including forests and shrublands. Moreover, while differences in R values are generally small across most land covers, the scene-mapping methods also maintain comparatively high correlations across the majority of surface classes.

As shown in Fig. 9, retrieval performance exhibits distinct regional and latitudinal contrasts. In low-latitude regions, S-LUT and S-Poly achieve RMSEs of 32.2 and 33.0 $W m^{-2}$, respectively, compared with 34.8 $W m^{-2}$ for Wang2023 and 36.0–38.1 $W m^{-2}$ for the other methods. S-Poly shows the smallest bias in this region, at 0.6 $W m^{-2}$. In mid-latitude regions, S-LUT and S-Poly achieve RMSEs of 23.9 and 23.3 $W m^{-2}$, respectively, which are lower than those of both traditional LUT methods and the three parameterization models.

In the polar regions, all models display pronounced negative biases, highlighting the persistent challenge of longwave retrieval under cold, dry, and radiatively weak conditions. Very low atmospheric moisture and complex surface–atmosphere thermal structures increase the difficulty of LWDR retrieval under these conditions. Nevertheless, the scene-mapping approaches remain comparatively stable. S-Poly achieves the lowest RMSE of 30.1 $W m^{-2}$, followed by Wang2009 at 30.5 $W m^{-2}$ and S-LUT at 30.9 $W m^{-2}$. The relatively similar performance among several methods indicates that polar retrieval remains challenging for all approaches.

On the Tibetan Plateau, known as the “Third Pole” with high elevation and complex climate, retrieval remained challenging for all methods. Even so, S-LUT achieves the lowest RMSE of 32.4 $W m^{-2}$, followed by Wang2023 at 33.6 $W m^{-2}$ and S-Poly at 34.5 $W m^{-2}$. T-Global shows the largest RMSE among the LUT-based approaches, reaching 40.8 $W m^{-2}$. The scene-mapping methods therefore remain among the better-performing approaches across the tested regions, although polar and high-elevation retrieval remains challenging.

4.2.3. Spatial distribution and retrieval consistency

Fig. 10 further compares the spatial distributions of the seven retrieval methods over a representative MODIS scene. The collocated CERES-SSF Model B observations provide an independent satellite reference for the same scene. Because CERES-SSF has a substantially larger footprint than MODIS, its spatial sampling is coarser and sparser. Nevertheless, the broad LWDR distribution represented by CERES-SSF is consistent with the main regional patterns reproduced by the MODIS-based retrievals.

At the common 5-km MODIS grid, the retrieved LWDR fields retain spatial textures related to the underlying satellite inputs, including the BT, ST, and TCWV distributions. The four LUT-based methods reproduce similar regional structures, while differences appear mainly in the finer-scale spatial variability. S-LUT and S-Poly show relatively continuous distributions, whereas T-Global and T-Cascade exhibit somewhat stronger local variation. Wang2023 also captures the main regional gradient, with a smoother spatial pattern that is consistent with its dependence on ST and TCWV.

More pronounced horizontal striping is visible in the Tang2008 and Wang2009 retrievals. Similar scan-line-correlated structures are also present in several native MOD02SSH radiance channels used by these implementations (Fig. 11), indicating that the Level-1B inputs contribute substantially to the retrieved patterns. Tang2008 directly combines multiple TOA radiances with coefficients of different signs, while Wang2009 further includes radiance products and ratios. Small band-dependent variations in the Level-1B radiances can therefore propagate through these empirical formulations and become more visible in the retrieved LWDR. This behavior is particularly associated with the radiance patterns in L34 for Tang2008 and in L27 and L34 for Wang2009. The observed striping is therefore more appropriately interpreted as the combined effect of the native radiance structure, the adopted model formulations, and the specific scene, rather than as an intrinsic limitation of the original Tang and Li (2008) or Wang and Liang (2009) algorithms.

4.3. Impact of input data sources on retrieval performance

Several existing products have been developed using the scheme of Wang et al. (2023) and Wang et al. (2020) as an intermediate or final component, most of which employ ERA5 TCWV together with MODIS-derived ST (Du et al., 2025; Du et al., 2024; Letu et al., 2022). To

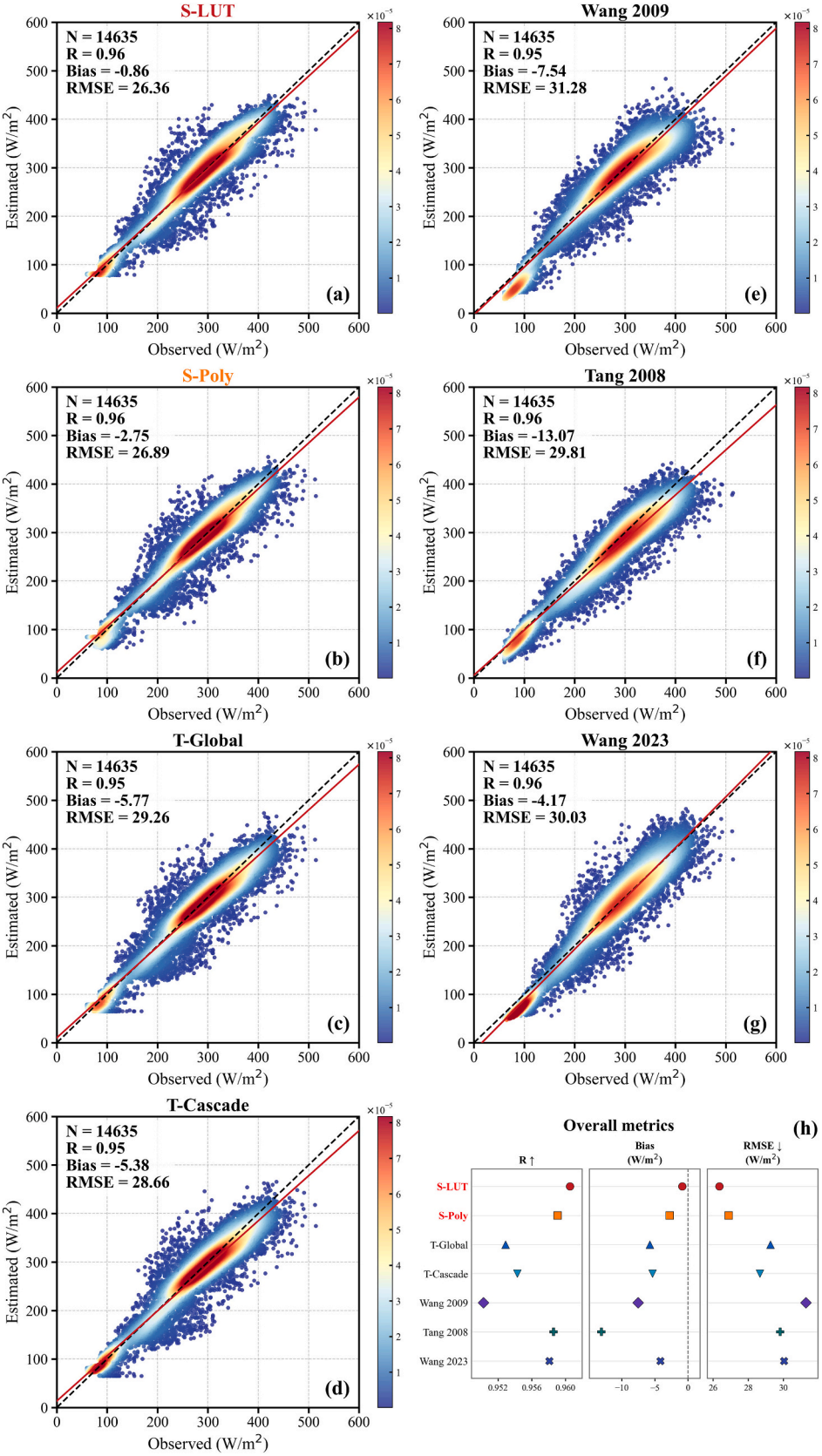


Fig. 7. Validation of LWDR retrieval methods against ground-based observations using MODIS data: S-LUT (a), S-Poly (b), T-Global (c), T-Cascade (d), Wang2009 (e), Tang2008 (f), and Wang2023 (g), with an overall comparison of R, bias, and RMSE across the seven methods (h).

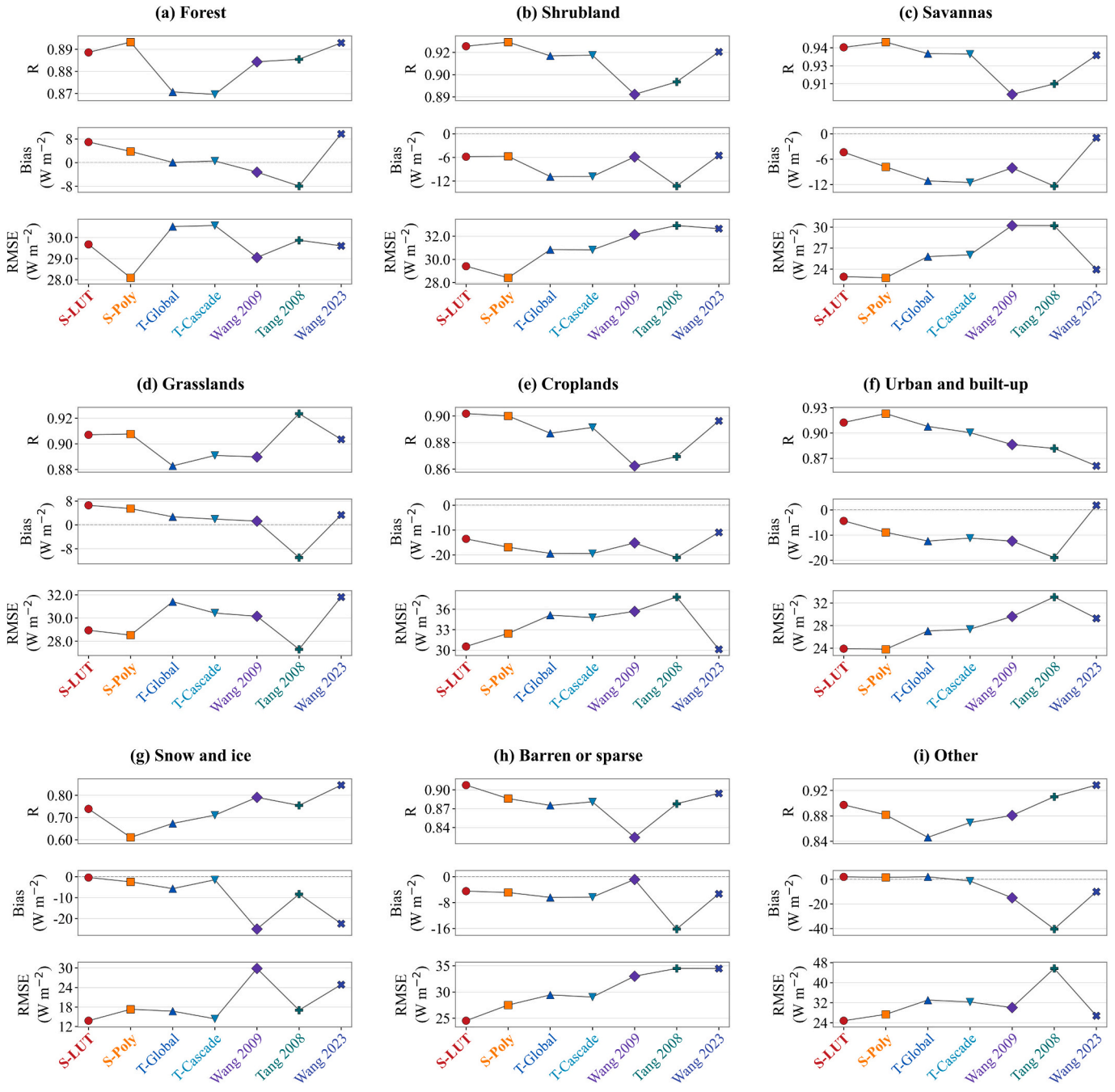


Fig. 8. Performance comparison of seven LWDR retrieval methods across different land-cover types in terms of R, bias, and RMSE.

ensure consistency with these applications and to evaluate the adaptability of the new framework under mixed-source conditions, the same ERA5–MODIS mixed-source configuration (BTs derived from MOD/MYD02SSH, ST from MOD/MYD06, and ERA5 TCWV) was adopted for validation (Fig. 12).

Under the mixed-source configuration, S-LUT achieves the lowest RMSE of 22.48 W m^{-2}, with a bias of 0.52 W m^{-2}. Wang2023 also remains highly competitive, with an RMSE of 23.29 W m^{-2} and a bias of 0.50 W m^{-2}. S-Poly yields an RMSE of 24.13 W m^{-2} and a bias of −0.51 W m^{-2}. Its slightly larger RMSE is mainly associated with increased dispersion in the low-LWDR range. This may reflect both the limited flexibility of the current first-order polynomial mapping under these conditions and the still limited representation of cold–dry polar states in the LUT. Thus, S-LUT, S-Poly, and Wang2023 all show small systematic biases, although their overall errors differ. The traditional LUT methods, T-Global and T-Cascade, produce RMSEs of 26.94 and 26.11 W m^{-2} and biases of −6.09 and −5.78 W m^{-2}, respectively. Their stronger negative biases, particularly in the low-LWDR range, also suggest that the current LUT does not yet fully represent extreme cold–dry atmospheric states. S-LUT therefore achieves the lowest retrieval error under the mixed-source configuration.

The scene-mapping framework uses ST and TCWV primarily as scene constraints to restrict retrievals to locally consistent atmospheric–surface states. ERA5 TCWV provides a useful large-scale moisture constraint, but its coarse spatial resolution may smooth local humidity gradients. When the scene window is expanded around this smoothed moisture state, the constraint may become less specific and include a broader range of atmospheric conditions. Despite this limitation, the

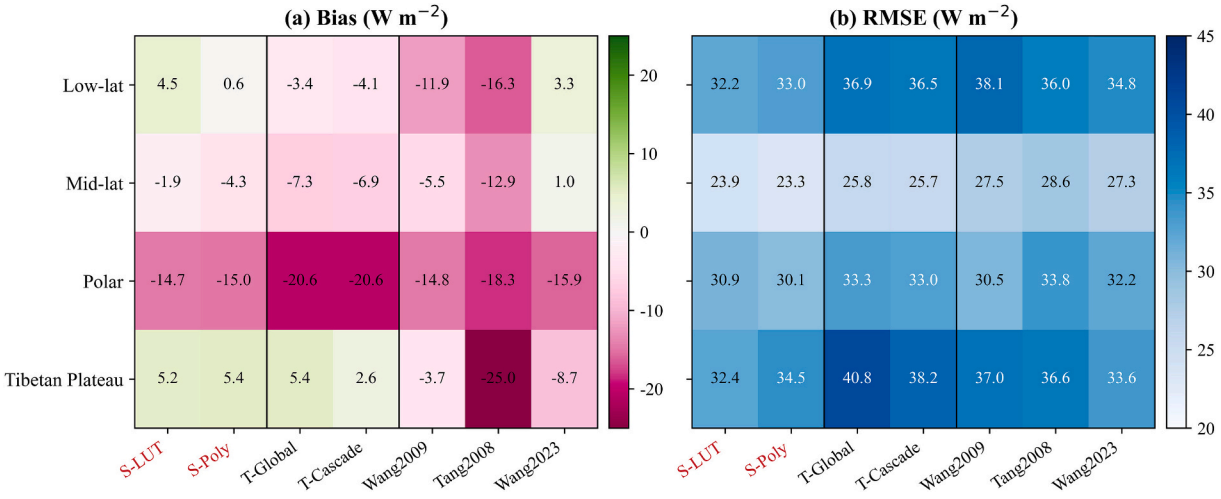


Fig. 9. Bias (a) and RMSE (b) of different retrieval strategies across four regional groups.

results show that the framework remains applicable under the mixed-source configuration. The expansion settings used here were not specifically optimized for the ERA5–MODIS configuration. For applications using different auxiliary data sources, the scene-window parameters can be tuned using independent parameter-tuning samples to account for their spatial resolution and uncertainty characteristics without changing the overall retrieval framework.

The ocean subset was further evaluated to examine retrieval performance under relatively homogeneous surface conditions (Fig. 13). Over ocean, the relatively uniform surface emissivity reduces surface-related variability, making LWDR more closely associated with atmospheric moisture conditions. This is particularly relevant to the mixed-source configuration used here, in which ERA5 TCWV provides the primary constraint on atmospheric moisture state. All three methods show clear agreement with the ground measurements, although systematic underestimation remains at higher LWDR values. S-LUT achieves the lowest RMSE and the smallest absolute bias, while S-Poly shows the highest correlation. Wang2023 yields an RMSE close to that of S-Poly. Compared with Wang2023, S-LUT reduces RMSE by about 7.6%, indicating that the scene constraint can provide additional benefit even when ERA5 TCWV already supplies a strong large-scale moisture-state constraint.

A footprint-scale intercomparison was further conducted using collocated CERES-SSF Model B clear-sky LWDR for a Terra overpass on 28 April 2018 (Fig. 14). To account for the different spatial resolutions, the MODIS-based retrievals were aggregated to each CERES footprint using the CERES point spread function (PSF) as spatial weights. Only footprints jointly valid for CERES-SSF and all three retrieval methods were retained. The spatial distributions show that S-LUT, S-Poly, and Wang2023 closely reproduce the along-track LWDR variations represented by CERES-SSF. The footprint-scale comparisons also show strong consistency, with $R = 0.99$ for all three methods. S-Poly shows the smallest RMSE and bias relative to CERES-SSF, followed by S-LUT, while Wang2023 also maintains close agreement. Positive retrieval-minus-CERES biases are observed for all three methods, whereas much smaller biases are obtained against ground observations under the same mixed-source configuration. CERES-SSF Model B has also been reported to underestimate clear-sky downward longwave flux (Kratz et al., 2020). The CERES-SSF comparison is therefore used primarily as a complementary assessment of footprint-scale spatial consistency.

5. Discussion

5.1. Use of brightness temperature instead of radiance in statistical retrievals

Many satellite statistical and hybrid approaches that directly use TOA thermal observations have traditionally been formulated in radiance space, where radiance is both the direct radiative-transfer quantity and a standard Level-1B sensor product.

In contrast to traditional radiance-based algorithms, this study adopts BT as the primary input variable because it provides a physically interpretable Kelvin-scale representation of calibrated thermal-band radiance. For each MODIS thermal band, BT was defined from the SRF-integrated Planck relationship using the corresponding band-specific SRF (Berk, 2008). The same SRFs were used in the MODTRAN simulations. Under this band-specific definition, the radiance-to-BT transformation is deterministic and numerically reversible. It therefore preserves the radiometric information content. This temperature-domain representation also facilitates future multi-sensor extensions, particularly the joint use of thermal-infrared and passive-microwave observations (Chen et al., 2022), but their applicability to LWDR remains to be tested. Accordingly, the reversibility discussed here is sensor specific; extension to other sensors would require their sensor-specific SRFs and corresponding radiative-transfer simulations.

5.2. Supplementary validation using machine learning

As a supplementary validation, a machine-learning benchmark was introduced to examine whether global tree-ensemble mappings without explicit scene constraints could match or surpass the proposed framework when using the same predictor set. Four representative tree-ensemble models were evaluated: XGBoost, LightGBM, ExtraTrees, and Random Forest (Breiman, 2001; Chen and Guestrin, 2016; Geurts et al., 2006; Ke et al., 2017). Random Forest provides a classical and widely adopted bagging-based baseline, while ExtraTrees applies stronger randomization during tree construction. XGBoost represents a high-performing gradient-boosting method, and LightGBM provides a computationally efficient gradient-boosting implementation.

All four models were developed using the MODTRAN-based LUT described in Section 3.1. The predictors were VZ, ST, TCWV, and the simulated MODIS BTs of bands 29, 31, 32, and 33. Simulated LWDR was used as the target variable. The LUT samples were randomly divided using a fixed random seed (random_state = 42), with 85% used for

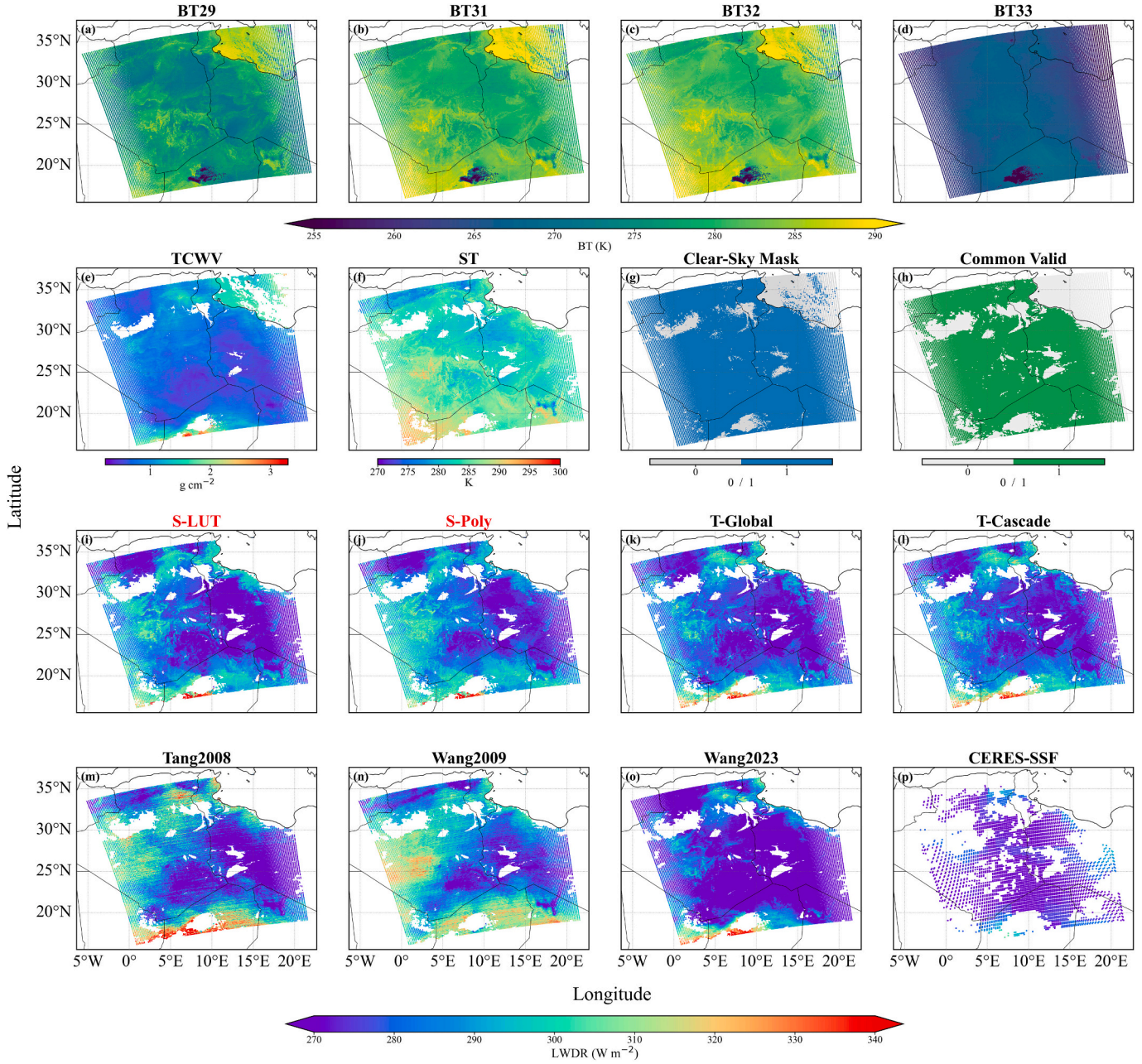


Fig. 10. Spatial comparison of MODIS inputs, clear-sky screening, LWDR retrievals, and CERES-SSF observations at 21:35 UTC on 4 December 2018.

model training and 15% used for internal validation. Each model was tuned separately using the same training–validation split, and its hyperparameters were selected according to performance on the internal validation set.

After model development, the four trained models were independently evaluated using actual MODIS observations and ground-based LWDR measurements under the same MODIS-only input configuration as in Section 4.2. Specifically, BTs were obtained from MOD02SSH, ST from MOD11, and TCWV from MOD05, while the station measurements served as the LWDR reference. The ground-based matchup data were not used for model training or hyperparameter selection.

Under this independent observational evaluation, the four machine-learning models achieved R values of 0.94–0.96, biases of −5.46 to −3.33 W m^{-2}, and RMSEs of 28.09–32.28 W m^{-2} (Fig. 15). LightGBM achieved the lowest RMSE among the machine-learning models, with $R = 0.96$, a bias of −3.33 W m^{-2}, and an RMSE of 28.09 W m^{-2}. XGBoost and ExtraTrees produced similar RMSEs of 28.34 and 28.42 W m^{-2}, respectively, whereas Random Forest produced the largest RMSE of 32.28 W m^{-2}.

Although the four tree-ensemble models provide reasonably accurate LWDR retrievals using the same predictors, their performance remains lower than that of the scene-mapping approaches under the same MODIS input configuration (Fig. 7). S-LUT and S-Poly achieve lower RMSEs than all four machine-learning models, while S-LUT also provides better control of systematic bias. These results suggest that restricting the retrieval to locally consistent surface–atmosphere states offers additional benefits over the tested data-driven models using the same input variables.

6. Conclusion

This paper introduces a scene-mapped LUT framework for clear-sky LWDR retrieval directly from brightness temperatures. The framework uses ST and TCWV to define scene-specific LUT subsets, thereby

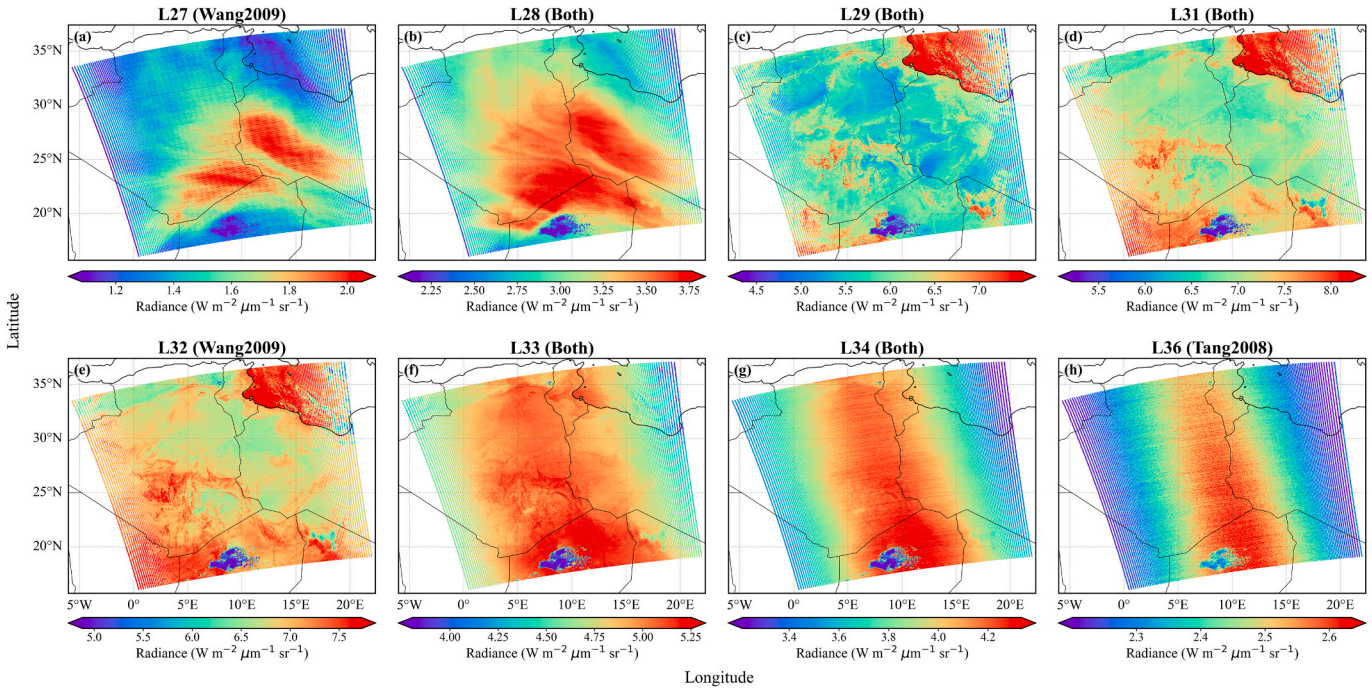


Fig. 11. Spatial distributions of the MODIS TOA radiance channels used by Wang2009 and Tang2008.

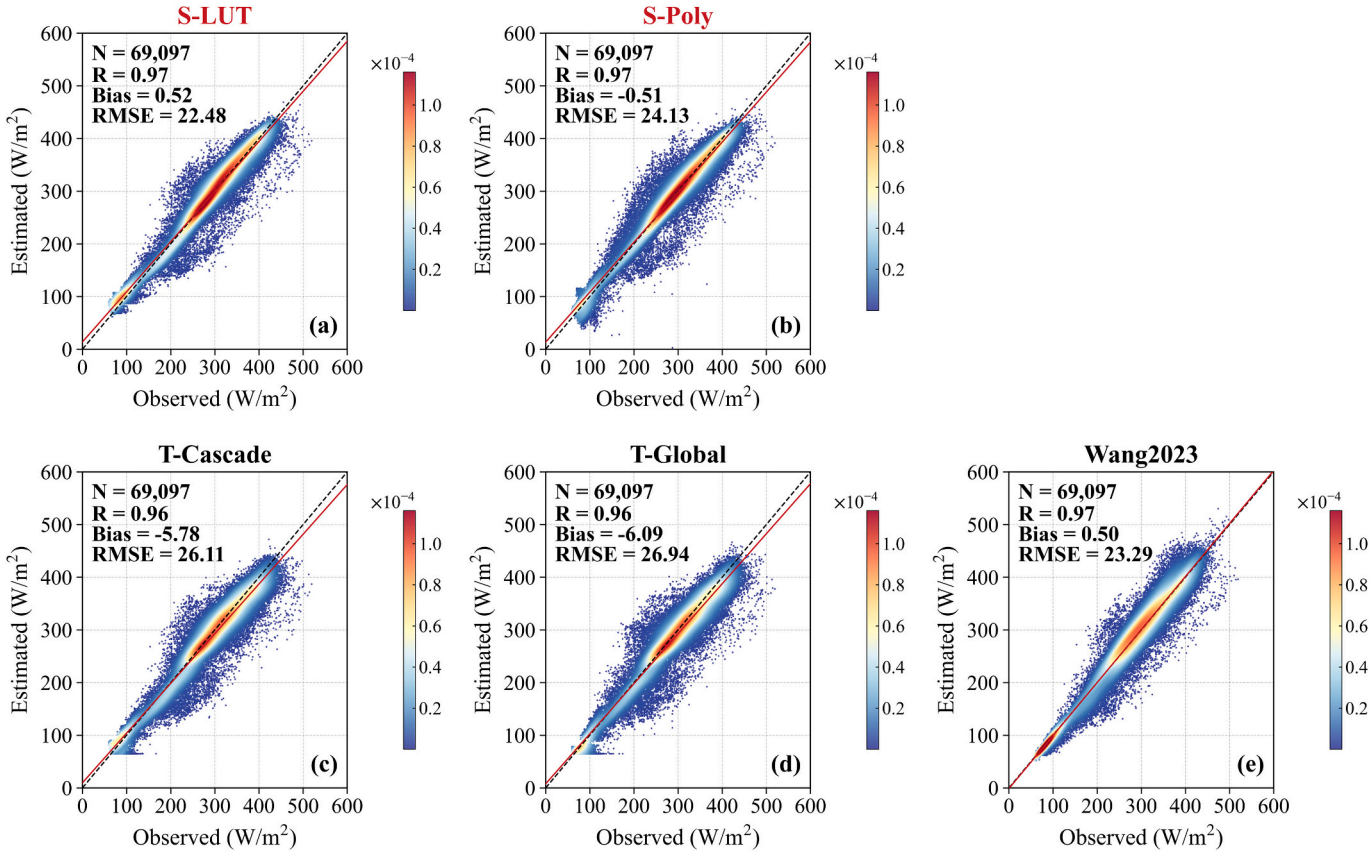


Fig. 12. Mixed-source validation of LWDR retrievals for S-LUT (a), S-Poly (b), T-Cascade (c), T-Global (d), and Wang2023 (e), using MOD/MYD06-derived ST and ERA5 TCWV.

restricting spectral matching to locally consistent surface–atmosphere states. Two implementations, S-LUT and S-Poly, were developed, and independent simulation validation confirmed their stable and reliable retrieval performance.

Under MODIS-based validation, S-LUT and S-Poly achieved RMSEs of 26.36 and 26.89 W m^{-2}, with biases of −0.86 and −2.75 W m^{-2}, respectively, outperforming both representative clear-sky parameterization models and traditional LUT-based approaches. Relative to

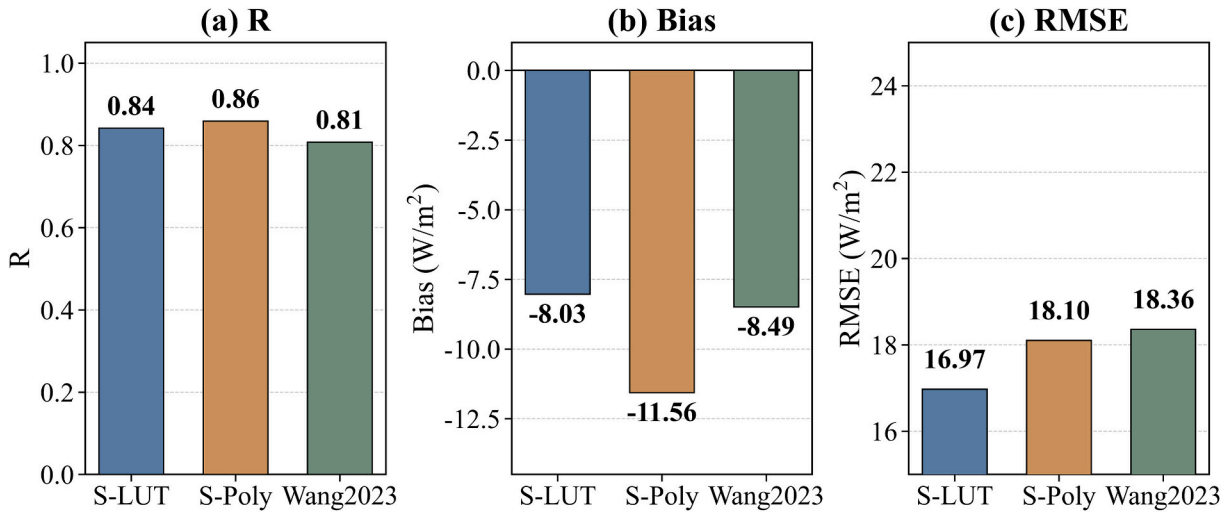


Fig. 13. Ocean-specific validation of LWDR retrievals under the mixed-source configuration.

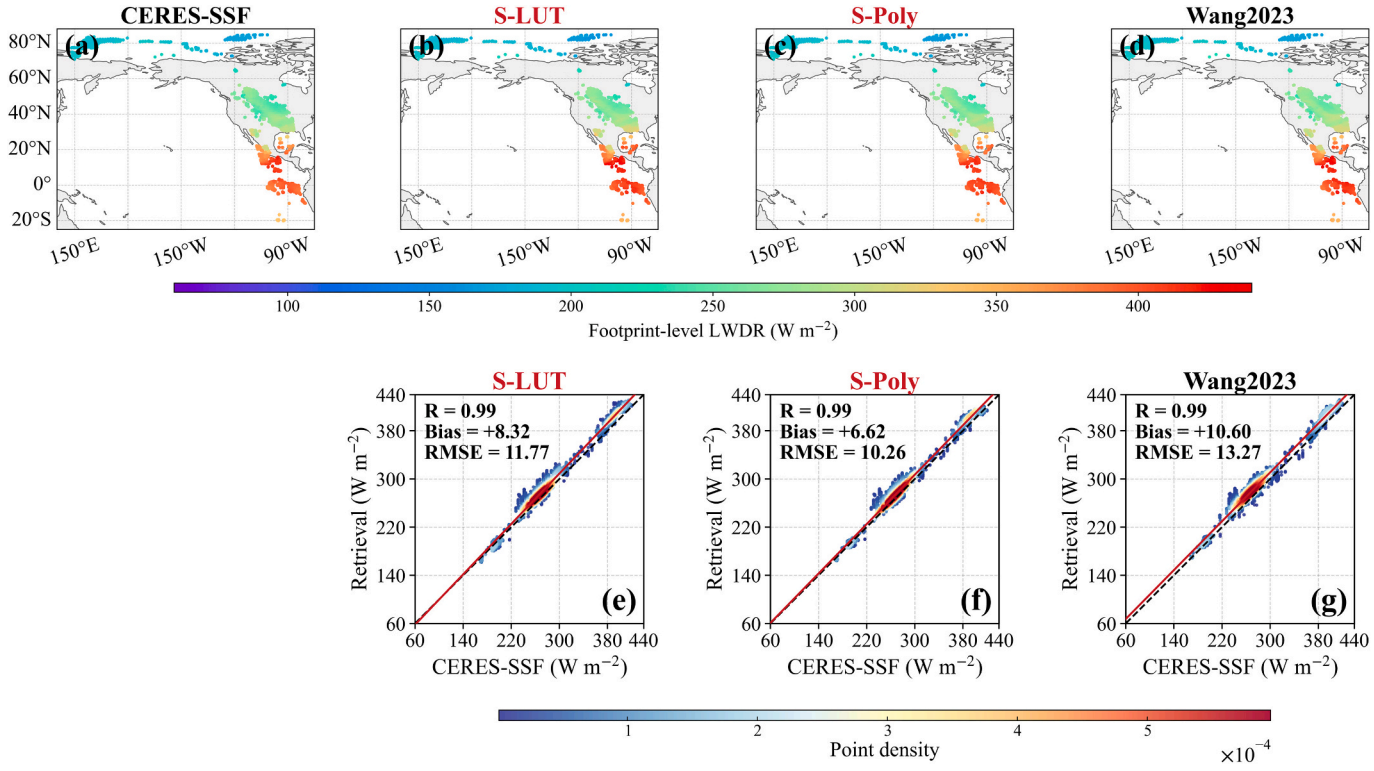


Fig. 14. Footprint-scale intercomparison of mixed-source LWDR retrievals with collocated CERES-SSF Model B clear-sky LWDR on 28 April 2018.

Wang2023, their RMSEs were reduced by approximately 12.2% and 10.5%. Under the mixed MODIS–ERA5 configuration, S-LUT again achieved the lowest RMSE of 22.48 W m^{-2}, compared with 23.29 W m^{-2} for Wang2023 and 24.13 W m^{-2} for S-Poly. Considering the results across the tested input configurations, S-LUT shows more consistent and stable performance and is therefore recommended as the preferred implementation for practical retrieval. S-Poly also performs well, but its local regression is more sensitive to the representativeness of scene-specific samples and may become less stable near sparsely sampled state-space boundaries. This limitation may become more apparent under extreme cold–dry conditions, particularly in the polar regions and over the Tibetan Plateau. The limited representation of such conditions in the current TIGR-based LUT therefore remains an important source of uncertainty, motivating further enrichment of cold–dry atmospheric profiles and refinement of moisture constraints under very low-TCWV conditions.

Overall, the proposed approach provides an accurate, efficient, and physically interpretable solution for clear-sky LWDR estimation. Although the present implementation focuses on clear-sky conditions, the scene-mapping architecture is not inherently restricted to clear skies. By incorporating cloud properties as additional scene descriptors with corresponding radiative-transfer simulations, the framework has the potential to be extended to cloudy-sky retrieval. Its flexible scene definition and brightness-temperature-based implementation may also facilitate adaptation to different sensors and input configurations, providing a potential basis for the synergistic use of thermal infrared and

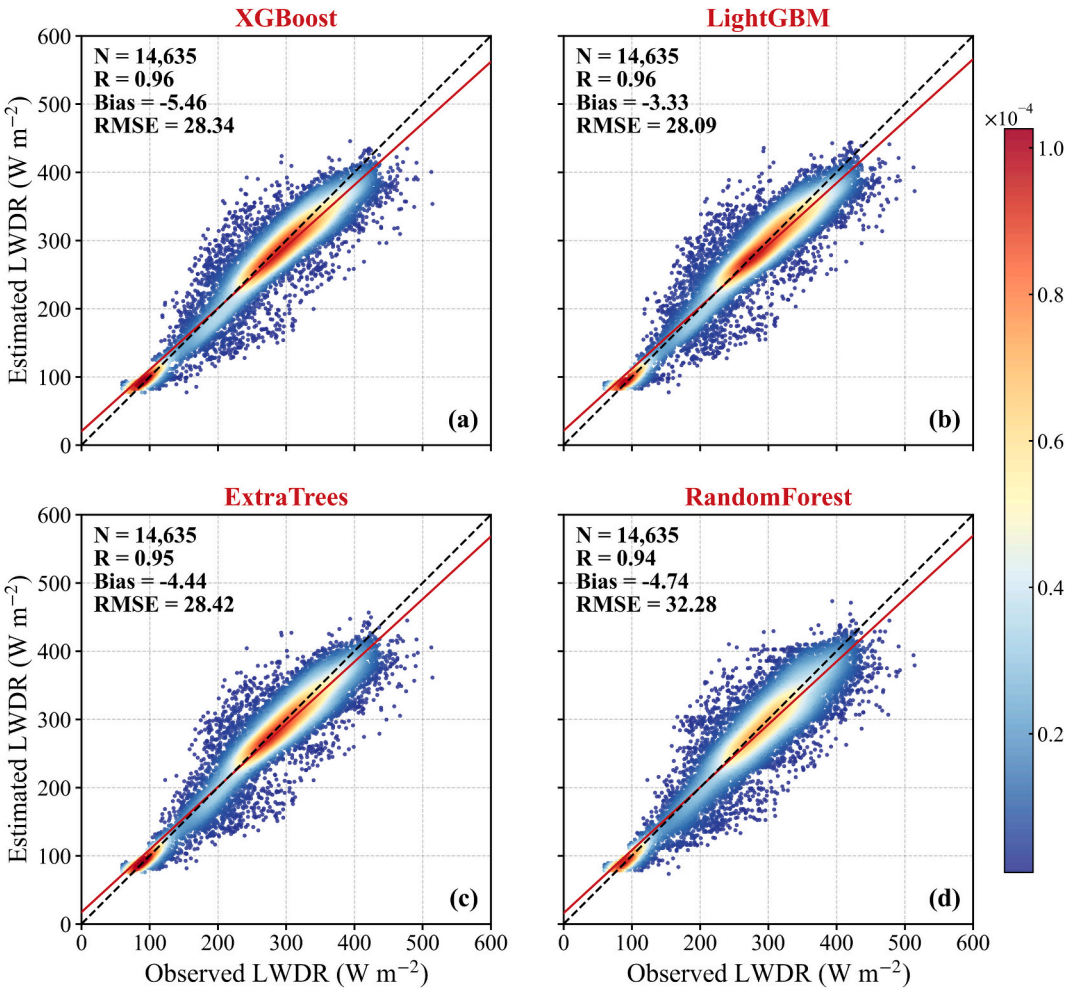


Fig. 15. External validation of LWDR retrievals from four machine-learning models using the independent MODIS-based dataset and the same input configuration as in Section 4.2: (a) XGBoost, (b) LightGBM, (c) ExtraTrees, and (d) Random Forest.

microwave observations. Building on the clear-sky foundation established here, future work will focus on the development of cloudy-sky and ultimately integrated all-sky LWDR retrieval.

CRediT authorship contribution statement

Yihan Du: Writing – original draft, Visualization, Validation, Methodology, Conceptualization. **Tianxing Wang:** Writing – review & editing, Supervision, Funding acquisition, Conceptualization. **Yi Zheng:** Writing – review & editing, Supervision. **Dahui Li:** Writing – review & editing, Methodology, Formal analysis. **Yuyang Xian:** Writing – review & editing, Visualization, Funding acquisition. **Feiyao Gao:** Writing – review & editing, Visualization. **Stefan A. Buehler:** Writing – review & editing, Supervision.

Declaration of competing interest

The authors declare that they have no known competing financial interests or personal relationships that could have appeared to influence the work reported in this paper.

Acknowledgments

This work was carried out under the co-funding of the National Natural Science Foundation of China Grant No. 424B2007, No. 42371342, the Fundamental Research Funds for the Central Universities, Sun Yat-sen University, No. 24lgzy001, and the Science and Technology Planning Project of Guangdong Province, No. 2024A1111120008. The first author extends sincere gratitude to the University of Hamburg for their invaluable support and resources provided during the author's visit.

Data availability

Data will be made available on request.

References

Aires, F., Prigent, C., 2007. Sampling techniques in high-dimensional spaces for the development of satellite remote sensing database. J. Geophys. Res. Atmos. 112.
Beck, H.E., Zimmermann, N.E., McVicar, T.R., Vergopolan, N., Berg, A., Wood, E.F., 2018. Present and future Koppen-Geiger climate classification maps at 1-km resolution. Sci. Data 5, 180214.
Berk, A., 2008. Analytically derived conversion of spectral band radiance to brightness temperature. J. Quant. Spectrosc. Radiat. Transf. 109, 1266–1276.
Berk, A., Conforti, P., Hawes, F., 2015. An accelerated line-by-line option for MODTRAN (R) combining on-the-fly generation of line center absorption within 0.1 cm-1 bins and pre-computed line tails. In: Conference on Algorithms and Technologies for Multispectral, Hyperspectral, and Ultraspectral Imagery XXI (Baltimore, MD).
Breiman, L., 2001. Random forests. Mach. Learn. 45, 5–32.
Chauhan, M.K., Singh, N., Singh, J., Rajput, A., Nandan, H., Rajeev, K., Kumar, N.V.P.K., 2025. Radiative fluxes over the Himalayan region: evaluating the parameterization schemes and exploring the potential of the XGBoost machine learning tool for downward longwave radiation. J. Geophys. Res. Atmos. 130.
Chedin, A., Scott, N.A., Wahiche, C., Moulinier, P., 1985. The improved initialization inversion method: a high resolution physical method for temperature retrievals from satellites of the TIROS-N series. J. Clim. Appl. Meteorol. 24, 128–143.

Chen, T., Guestrin, C., 2016. XGBoost: a scalable tree boosting system. In: Proceedings of the 22nd ACM SIGKDD International Conference on Knowledge Discovery and Data Mining. Association for Computing Machinery, San Francisco, California, USA, pp. 785–794.
Chen, Z.W., Jin, R., Li, Q.X., Zhao, G.H., Xiao, C.W., Lei, Z.Y., Huang, Y.H., 2022. Joint inversion algorithm of sea surface temperature from microwave and infrared brightness temperature. IEEE Trans. Geosci. Remote Sens. 60.
Cheng, J., Liang, S.L., Shi, J.C., 2020. Impact of air temperature inversion on the clear-sky surface downward longwave radiation estimation. IEEE Trans. Geosci. Remote Sens. 58, 4796–4802.
Cheng, J., Liang, S.L., Wang, W.H., Guo, Y.M., 2017. An efficient hybrid method for estimating clear-sky surface downward longwave radiation from MODIS data. J. Geophys. Res. Atmos. 122, 2616–2630.
Chevallier, F., Chédin, A., Chéruy, F., Morcrette, J.J., 2000. TIGR-like atmospheric-profile databases for accurate radiative-flux computation. Q. J. R. Meteorol. Soc. 126, 777–785.
Chevallier, F., Chéruy, F., Scott, N.A., Chédin, A., 1998. A neural network approach for a fast and accurate computation of a longwave radiative budget. J. Appl. Meteorol. 37, 1385–1397.
Cronin, M.F., Anderson, N.D., Zhang, D.X., Berk, P., Wills, S.M., Serra, Y., Kohlman, C., Sutton, A.J., Honda, M.C., Kawai, Y., Yang, J., Thomson, J., Lawrence-Slavas, N., Eyre, J.R., Meinig, C., 2023. Pmel ocean climate stations as reference time series and research aggregate devices. Oceanography 36, 46–53.
Doelling, D.R., Sun, M., Nguyen, L.T., Nordeen, M.L., Haney, C.O., Keyes, D.F., Mlynczak, P.E., 2016. Advances in geostationary-derived longwave fluxes for the CERES synoptic (SYN1deg) product. J. Atmos. Ocean. Technol. 33, 503–521.
Driemel, A., Augustine, J., Behrens, K., Colle, S., Cox, C., Cuevas-Agulló, E., Denn, F.M., Duprat, T., Fukuda, M., Grobe, H., Haeffelin, M., Hodges, G., Hyett, N., Ijima, O., Kallis, A., Knap, W., Kustov, V., Long, C.N., Longenecker, D., Lupi, A., Maturilli, M., Mimouni, M., Ntsangwane, L., Ogihara, H., Olano, X., Olefs, M., Omori, M., Passamani, L., Pereira, E.B., Schmithüsen, H., Schumacher, S., Sieger, R., Tamlyn, J., Vogt, R., Vuilleumier, L., Xia, X., Ohmura, A., König-Langlo, G., 2018. Baseline Surface Radiation Network (BSRN): structure and data description (1992–2017). Earth Syst. Sci. Data 10, 1491–1501.
Du, Y., Wang, S., Wang, T., Zheng, Y., Xian, Y., Li, D., 2025. A 41-year global all-sky surface longwave radiation components dataset at 5 km and hourly resolution. Sci. Data 12, 1540.
Du, Y., Wang, T., Zhou, Y., Letu, H., Li, D., Xian, Y., 2024. Toward user-friendly all-sky surface longwave downward radiation from space: general scheme and product. Bull. Am. Meteorol. Soc. 105, E1303–E1319.
Dupont, J.C., Haeffelin, M., Drobinski, P., Besnard, T., 2008. Parametric model to estimate clear-sky longwave irradiance at the surface on the basis of vertical distribution of humidity and temperature. J. Geophys. Res. Atmos. 113.
Feng, C.J., Zhang, X.T., Wei, Y., Zhang, W.Y., Hou, N., Xu, J.W., Jia, K., Yao, Y.J., Xie, X. H., Jiang, B., Cheng, J., Zhao, X., 2020. Estimating surface downward longwave radiation using machine learning methods. Atmosphere 11.
Friedl, M.A., Sulla-Menashe, D., Tan, B., Schneider, A., Ramankutty, N., Sibley, A., Huang, X.M., 2010. MODIS Collection 5 global land cover: algorithm refinements and characterization of new datasets. Remote Sens. Environ. 114, 168–182.
Geurts, P., Ernst, D., Wehenkel, L., 2006. Extremely randomized trees. Mach. Learn. 63, 3–42.
Guo, M., Cheng, J., Zeng, Q., 2024. A data-driven model for estimating clear-sky surface longwave downward radiation over polar regions. IEEE Trans. Geosci. Remote Sens. 62.
Gupta, S.K., Kratz, D.P., Stackhouse, P.W., Wilber, A.C., Zhang, T.P., Sothcott, V.E., 2010. Improvement of surface longwave flux algorithms used in CERES processing. J. Appl. Meteorol. Climatol. 49, 1579–1589.
Hersbach, H., Bell, B., Berrisford, P., Hirahara, S., Horanyi, A., Munoz-Sabater, J., Nicolas, J., Peubey, C., Radu, R., Schepers, D., Simmons, A., Soci, C., Abdalla, S., Abellan, X., Balsamo, G., Bechtold, P., Biavati, G., Bidlot, J., Bonavita, M., De Chiara, G., Dahlgren, P., Dee, D., Diamantakis, M., Dragani, R., Flemming, J., Forbes, R., Fuentes, M., Geer, A., Haimberger, L., Healy, S., Hogan, R.J., Holm, E., Janiskova, M., Keeley, S., Laloyaux, P., Lopez, P., Lupu, C., Radnoti, G., de Rosnay, P., Rozum, I., Vamborg, F., Villaume, S., Thepaut, J.N., 2020. The ERA5 global reanalysis. Q. J. R. Meteorol. Soc. 146, 1999–2049.
Idso, S.B., 1981. A set of equations for full spectrum and 8- to 14-μm and 10.5- to 12.5-μm thermal radiation from cloudless skies. Water Resour. Res. 17, 295–304.
Jiao, Z.H., Mu, X.H., 2022. Global validation of clear-sky models for retrieving land-surface downward longwave radiation from MODIS data. Remote Sens. Environ. 271, 112903.
Ke, G.L., Meng, Q., Finley, T., Wang, T.F., Chen, W., Ma, W.D., Ye, Q.W., Liu, T.Y., 2017. LightGBM: a highly efficient gradient boosting decision tree. In: Advances in Neural Information Processing Systems 30 (Nips 2017), pp. 3146–3154.
King, M.D., Platnick, S., Menzel, W.P., Ackerman, S.A., Hubanks, P.A., 2013. Spatial and temporal distribution of clouds observed by MODIS onboard the Terra and Aqua satellites. IEEE Trans. Geosci. Remote Sens. 51, 3826–3852.
Kratz, D.P., Gupta, S.K., Wilber, A.C., Sothcott, V.E., 2020. Validation of the CERES edition-4A surface-only flux algorithms. J. Appl. Meteorol. Climatol. 59, 281–295.
Lelli, L., Vountas, M., Khosravi, N., Burrows, J.P., 2023. Satellite remote sensing of regional and seasonal Arctic cooling showing a multi-decadal trend towards brighter and more liquid clouds. Atmos. Chem. Phys. 23, 2579–2611.
Letu, H., Nakajima, T.Y., Wang, T., Shang, H., Ma, R., Yang, K., Baran, A.J., Riedi, J., Ishimoto, H., Yoshida, M., Shi, C., Khatri, P., Du, Y., Chen, L., Shi, J., 2022. A new benchmark for surface radiation products over the East Asia-Pacific region retrieved from the Himawari-8/AHI next- generation geostationary satellite. Bull. Am. Meteorol. Soc. 103, E873–E888.
Li, D., Wang, T., Zheng, X., Zhang, P., Zheng, L., Leng, W., Du, Y., Chen, L., Zhang, W., 2024. Multi-dimensional matrix MAPping (MDMAP): a new algorithm framework to derive top-of-atmosphere outgoing longwave radiation from space. Remote Sens. Environ. 304, 114031.
Liang, S.L., Cheng, J., Jia, K., Jiang, B., Liu, Q., Xiao, Z.Q., Yao, Y.J., Yuan, W.P., Zhang, X.T., Zhao, X., Zhou, J., 2021. The global land surface satellite (GLASS) product suite. Bull. Am. Meteorol. Soc. 102, E323–E337.
Liang, S.L., Wang, D.D., He, T., Yu, Y.Y., 2019. Remote sensing of Earth's energy budget: synthesis and review. Int. J. Digit. Earth 12, 737–780.
Liang, S.L., Wang, K.C., Zhang, X.T., Wild, M., 2010. Review on estimation of land surface radiation and energy budgets from ground measurement, remote sensing and model simulations. IEEE J. Sel. Top. Appl. Earth Obs. Remote Sens. 3, 225–240.
Loeb, N.G., Kato, S., Loukachine, K., Manalo-Smith, N., 2005. Angular distribution models for top-of-atmosphere radiative flux estimation from the clouds and the earth's radiant energy system instrument on the Terra satellite. Part I: methodology. J. Atmos. Ocean. Technol. 22, 338–351.
Loeb, N.G., Kato, S., Loukachine, K., Manalo-Smith, N., Doelling, D.R., 2007. Angular distribution models for top-of-atmosphere radiative flux estimation from the clouds and the earth's radiant energy system instrument on the Terra satellite. Part II: validation. J. Atmos. Ocean. Technol. 24, 564–584.
Lopes, F.M., Dutra, E., Trigo, I.F., Wild, M., 2024. Evaluation of downward surface longwave flux estimates using Meteosat cloud observations. J. Geophys. Res. Atmos. 129, e2023JD040306.
Ma, Y., Xie, Z., Chen, Y., Liu, S., Che, T., Xu, Z., Shang, L., He, X., Meng, X., Ma, W., Xu, B., Zhao, H., Wang, J., Wu, G., Li, X., 2024. Dataset of spatially extensive long-term quality-assured land–atmosphere interactions over the Tibetan Plateau. Earth Syst. Sci. Data 16, 3017–3043.
Mangum, L.J., Freitag, H.P., McPhaden, M.J., 1994. TOGA-TAO array sampling schemes and sensor evaluations. In: Proceedings of OCEANS'94, *2*, pp. II/402–II/406.
Meerdink, S.K., Hook, S.J., Roberts, D.A., Abbott, E.A., 2019. The ECOSTRESS spectral library version 1.0. Remote Sens. Environ. 230, 111196.
Novick, K.A., Biederman, J.A., Desai, A.R., Litvak, M.E., Moore, D.J.P., Scott, R.L., Torn, M.S., 2018. The AmeriFlux network: a coalition of the willing. Agric. For. Meteorol. 249, 444–456.
Pace, G., di Sarra, A., Quaglia, F.C., Ciardini, V., Di Iorio, T., Iaccarino, A., Meloni, D., Muscari, G., Scarchilli, C., 2024. Verification of parameterizations for clear sky downwelling longwave irradiance in the Arctic. Atmos. Meas. Tech. 17, 1617–1632.
Prata, A., 1996. A new long-wave formula for estimating downward clear-sky radiation at the surface. Q. J. R. Meteorol. Soc. 122, 1127–1151.
Reichstein, M., Camps-Valls, G., Stevens, B., Jung, M., Denzler, J., Carvalhais, N., Prabhat, 2019. Deep learning and process understanding for data-driven earth system science. Nature 566, 195–204.
Ru, C., Duan, S.-B., Jiang, X.-G., Li, Z.-L., Huang, C., Liu, M., 2023. An extended SW-TES algorithm for land surface temperature and emissivity retrieval from ECOSTRESS thermal infrared data over urban areas. Remote Sens. Environ. 290.
Servera, J.V., Alonso, L., Martino, L., Sabater, N., Verrelst, J., Camps-Valls, G., Moreno, J., 2019. Gradient-based automatic lookup table generator for radiative transfer models. IEEE Trans. Geosci. Remote Sens. 57, 1040–1048.
Stephens, G.L., Wild, M., Stackhouse, P.W., L'Ecuyer, T., Kato, S., Henderson, D.S., 2012. The global character of the flux of downward longwave radiation. J. Clim. 25, 2329–2340.
Su, W., Corbett, J., Eitzen, Z., Liang, L., 2015. Next-generation angular distribution models for top-of-atmosphere radiative flux calculation from CERES instruments: methodology. Atmos. Meas. Tech. 8, 611–632.
Tang, B., Li, Z.L., 2008. Estimation of instantaneous net surface longwave radiation from MODIS cloud-free data. Remote Sens. Environ. 112, 3482–3492.
Toller, G., Xiong, X.X., Sun, J.Q., Wenny, B.N., Geng, X., Kuyper, J., Angal, A., Chen, H. D., Madhavan, S., Wu, A.S., 2013. Terra and Aqua moderate-resolution imaging spectroradiometer collection 6 level 1B algorithm. J. Appl. Remote. Sens. 7.
Trigo, I.F., Barroso, C., Viterbo, P., Freitas, S.C., Monteiro, I.T., 2010. Estimation of downward long-wave radiation at the surface combining remotely sensed data and NWP data. J. Geophys. Res. Atmos. 115.
Vicent, J., Verrelst, J., Sabater, N., Alonso, L., Rivera-Caicedo, J.P., Martino, L., Muñoz-Marí, J., Moreno, J., 2020. Comparative analysis of atmospheric radiative transfer models using the Atmospheric Look-up table Generator (ALG) toolbox (version 2.0). Geosci. Model Dev. 13, 1945–1957.
Wan, Z.M., 2014. New refinements and validation of the collection-6 MODIS land-surface temperature/emissivity product. Remote Sens. Environ. 140, 36–45.
Wang, K.C., Dickinson, R.E., 2013. Global atmospheric downward longwave radiation at the surface from ground-based observations, satellite retrievals, and reanalyses. Rev. Geophys. 51, 150–185.
Wang, M., He, G., Hu, T., Yang, M., Zhang, Z., Zhang, Z., Wang, G., Li, H., Gao, W., Liu, X., 2024. Innovative hybrid algorithm for simultaneous land surface temperature and emissivity retrieval: case study with SDGSAT-1 data. Remote Sens. Environ. 315.
Wang, T., Wang, G., Shi, C., Du, Y., Letu, H., Zhang, W., Xue, H., 2023. Improved algorithm to derive all-sky longwave downward radiation from space: application to Fengyun-4A measurements. IEEE Trans. Geosci. Remote Sens. 61, 1–13.
Wang, T.X., Shi, J.C., Ma, Y., Letu, H., Li, X.C., 2020. All-sky longwave downward radiation from satellite measurements: general parameterizations based on LST, column water vapor and cloud top temperature. ISPRS J. Photogramm. Remote Sens. 161, 52–60.
Wang, T.X., Yan, G.J., Chen, L., 2012. Consistent retrieval methods to estimate land surface shortwave and longwave radiative flux components under clear-sky conditions. Remote Sens. Environ. 124, 61–71.

Wang, W.H., Liang, S.L., 2009. Estimation of high-spatial resolution clear-sky longwave downward and net radiation over land surfaces from MODIS data. Remote Sens. Environ. 113, 745–754.
Wang, W.H., Liang, S.L., 2010. A method for estimating clear-sky instantaneous land-surface longwave radiation with GOES sounder and GOES-R ABI data. IEEE Geosci. Remote Sens. Lett. 7, 708–712.
Weller, R.A., Lukas, R., Potemra, J., Plueddemann, A.J., Fairall, C., Bigorre, S., 2022. Ocean reference stations long-term, open-ocean observations of surface meteorology and air-sea fluxes are essential benchmarks. Bull. Am. Meteorol. Soc. 103, E1968–E1990.
Wild, M., Folini, D., Schär, C., Loeb, N., Dutton, E.G., König-Langlo, G., 2013. The global energy balance from a surface perspective. Clim. Dyn. 40, 3107–3134.
Xu, J., Liang, S., Ma, H., Chen, Y., Li, W., Ma, Y., Zhao, X., Jiang, B., Zhang, X., Guan, S., 2026. Joint estimation of global daily 1 km surface radiation budget components from MODIS observations (2000−2023) using conservation-constrained deep neural networks. Remote Sens. Environ. 333, 115135.
Xu, J., Liang, S., Ma, H., He, T., 2022. Generating 5 km resolution 1981–2018 daily global land surface longwave radiation products from AVHRR shortwave and longwave observations using densely connected convolutional neural networks. Remote Sens. Environ. 280, 113223.
Xu, J., Liang, S., Ma, H., He, T., Zhang, Y., Zhang, G., 2023. A daily 5-km all-sky sea-surface longwave radiation product based on statistically modified deep neural network and spatiotemporal analysis for 1981–2018. Remote Sens. Environ. 290, 113550.
Yu, G.R., Hirano, T., 2021. Review and future perspective of AsiaFlux. J. Agric. Meteorol. 77, 1.
Yu, S.S., Li, L., Cao, B., Zhang, H.L., Zhu, L., Xin, X.Z., Liu, Q.H., 2022. Surface downward longwave radiation estimation from new generation geostationary satellite data. Atmos. Res. 276, 106255.
Yu, S.S., Xin, X.Z., Liu, Q.H., Zhang, H.L., Li, L., 2019. An improved parameterization for retrieving clear-sky downward longwave radiation from satellite thermal infrared data. Remote Sens. 11, 425.
Zeng, Q., Cheng, J., Sun, H., Dong, S.Y., 2024. An integrated framework for estimating the hourly all-time cloudy-sky surface long-wave downward radiation for Fengyun-4A/AGRI. Remote Sens. Environ. 312, 114319.
Zhang, G.D., Ma, H., Liang, S.L., Jia, A.L., He, T., Wang, D.D., 2022. A machine learning method trained by radiative transfer model inversion for generating seven global land and atmospheric estimates from VIIRS top-of-atmosphere observations. Remote Sens. Environ. 279, 113132.
Zheng, X.P., Li, Z.L., Wang, T.X., Huang, H.B., Nerry, F., 2022. Determination of global land surface temperature using data from only five selected thermal infrared channels: method extension and accuracy assessment. Remote Sens. Environ. 268, 112774.
Zhou, W., Shi, J.C., Wang, T.X., Peng, B., Husi, L., Yu, Y.C., Zhao, R., 2019. New methods for deriving clear-sky surface longwave downward radiation based on remotely sensed data and ground measurements. Earth Space Sci. 6, 2071–2086.
Zhu, F., Li, X., Qin, J., Yang, K., Cuo, L., Tang, W., Shen, C., 2022. Integration of multisource data to estimate downward longwave radiation based on deep neural networks. IEEE Trans. Geosci. Remote Sens. 60, 1–15.